Electronic Supplementary Information

Heterostructured metal oxides realized by quenching-induced structural transformation

Changchun Ye,[1] Zhenghui Pan,[2,*] Qinghua Zhang,[3] Fang Yin,[4] Yanan Wang,[3,5] Yifei Li,[1] Guangxu Chen,[1] Jia Li,[4,*] Yongcai Qiu,[1,*] Geoffrey I. N. Waterhouse,[6] Lin Gu[3,*] Zhang Lin,[7] Lin Guo[8,*]

1 School of Environment and Energy, State Key Laboratory of Luminescent Materials and Devices, Guangdong Provincial Key Laboratory of Atmospheric Environment and Pollution Control, South China University of Technology, Guangzhou 510000, Guangdong, China

2 School of Materials Science and Engineering, Tongji University, Shanghai 201804, China

3 Key Laboratory for Renewable Energy, Beijing Key Laboratory for New Energy Materials and Devices, Laboratory of Advanced Materials and Electron Microscopy, Beijing National Laboratory for Condensed Matter Physics, Institute of Physics, Chinese Academy of Sciences, Beijing, 100190, China

4 Institute of Materials Research, Tsinghua Shenzhen International Graduate School, Tsinghua University, Shenzhen 518055, China

5 Songshan Lake Materials Laboratory, Dongguan, Guangdong, 523808 P. R. China

6 School of Chemical Sciences, The University of Auckland, Auckland 1142, New Zealand

7 School of Metallurgy and Environment, Central South University, Changsha 410083, PR China

8 School of Chemistry, Beijing Advanced Innovation Center for Biomedical Engineering, Beihang University, Beijing 100191, China

Experimental Section

Catalyst Characterization

The structure and crystallinity of the as-prepared samples were characterized by powder X-ray diffraction (XRD). The size and morphology of the samples were analyzed by using scanning electron microscopy (SEM) and transmission electron microscopy (TEM). X-ray photoelectron spectroscopy (XPS) data was collected on an ESCALAB MK II X-ray photoelectron spectrometer equipped with a Mg Kα excitation source. Raman spectroscopic analyses used a Horiba Jobin-YVON co-focal laser Raman system with a He-Ne 632 nm laser as the excitation source. Soft X-ray absorption spectroscopy (XAS) data was collected at Beamlines MCD-A and MCD-B (Soochow Beamline for Energy Materials) at NSRL. Electron paramagnetic resonance (EPR) spectroscopy was collected on Bruker A300-10/12. Specific surface area was measured using a JW-BK200C Surface Area and Pore size Analyzer (Beijing JWGBSci. & Tech. Co., Ltd.). The elemental composition of samples was determined using an inductively coupled plasma atomic emission spectrometer (ICP, SPECTRO ARCOS MV).

Electrochemical measurements

Catalyst inks were prepared by dispersing 5 mg of catalyst and 3 mg of conductive carbon black in 1 mL of a mixed solution containing 750 uL of deionized water, 200 uL of ethanol and 50 uL of a 5 wt.% Nafion solution. The inks were ultrasonicated for 1 h before use to achieve a homogeneous catalyst dispersion. All the electrochemical measurements were conducted on a CHI 760E electrochemical workstation (Chenhua, Shanghai). A three-electrode system was used, comprising a rotating disk glassy carbon electrode (5 mm in diameter) as the working electrode, a platinum foil as the counter electrode, and a Hg/HgO electrode as the reference electrode. To prepare the working electrode, 10 uL of catalyst ink was pipetted onto the surface of the glassy carbon electrode and dried at room temperature. The oxygen evolution reaction (OER) and oxygen reduction reaction (ORR) performance of the catalysts were evaluated by linear sweep voltammetry (LSV) in a 1 M KOH aqueous solution. Before each test, cyclic voltammetry (CV) was performed in the potential range of 1.0-1.7 V vs RHE to activate the catalysts. The LSV curves for OER were obtained in the potential range of 1.0-1.8 V vs. RHE using a scan rate of 5 mV s^{-1}. For ORR, the LSV curves were obtained in the potential range of 1.1-0.4 V vs. RHE using a scan rate of 5 mV s^{-1}. Electrochemical impedance spectroscopy (EIS)

measurements were performed at 1.60 V vs. RHE over a frequency range from 100 kHz to 0.1 Hz with a 5 mV AC dither. Stability tests used chronoamperometry (CA) at specified potential, with LSV curves also collected before and after the CA tests.

All potentials were converted to the reversible hydrogen electrode (RHE) using the following equation, which included an IR-drop potential correction due to the resistance of the electrolyte.

$$E\ (\text{vs. RHE}) = E\ (\text{vs. Hg/HgO}) + 0.098 + 0.059 \times \text{pH} \quad \text{(1)}$$

Tafel slopes were derived from the polarisation curves and overpotentials calculated according to the following Tafel equation,

$$\eta = a + b \log j \quad \text{(2)}$$

where η, a, b and j correspond to the overpotential, Tafel constant, Tafel slope and the current density, respectively. For OER, the overpotential (η) was calculated by subtracting 1.23 V (standard potential for water oxidation) from the measured potential using the following equation,

$$\eta = E\ (\text{vs. RHE}) - 1.23 \quad \text{(3)}$$

For the electrochemically active area studies, cyclic voltammograms were collected at various scan rates (10, 20, 40, 60, 80, 100 mV s^{-1}) over the potential range 1.1-1.2 V vs. RHE (i.e., in a non-Faradaic region). The double-layer current (ic) is equal to the product of the scan rate (ν) and the electrochemical double-layer capacitance (C_{DL}), as described by the equation,

$$ic = \nu C_{DL} \quad \text{(4)}$$

The slope of the linear ic-ν plot is equal to C_{DL}. The ECSA values were acquired by calculation according to equation,

$$ECSA = C_{DL}/C_s \quad \text{(5)}$$

where C_s is the specific capacitance (we used 40 μF cm^{-2} here which is typical for metal oxides).

Assembly and testing of aqueous zinc-air batteries

For the construction of aqueous zinc-air batteries (ZABs), the catalysts were loaded onto hydrophilic side of a carbon cloth to form an air cathode (mass loading about 1.0 mg cm^{-2}). A polished Zn foil served as the anode, and a mixed solution containing 6 M KOH and 0.2 M $Zn(CH_3COO)_2$ was used as the electrolyte. The charge and discharge polarization curves were recorded at 5 mV s^{-1} at room temperature. Cycling tests were conducted using charge-discharge cycles of 10 min discharge followed by 10 min charge at constant current density of 5 mA cm^{-2}. The full discharge tests were performed

by recording the change in voltage at a current density of 5 mA cm^{-2}, whilst the specific capacity was calculated accordingly to the mass of Zn consumed at the anode in the assembled batteries. Electrochemical impedance spectroscopy (EIS) measurements were carried out from 10^6 Hz to 0.1 Hz.

Assembly and testing of the solid-state flexible zinc-air batteries

The flexible solid-state Zn-air battery was fabricated using a Zn foil as anode, a polyvinyl alcohol (PVA) gel polymer as the solid electrolyte, and a carbon cloth loaded with $NiMoO_4$-Fe-5th catalyst as the air electrode (mass loading about 1.0 mg cm^{-2}). To prepare the PVA solid electrolyte, 1.6 g of PVA was dissolved in 16 mL of water and the resulting solution stirred at 90 °C for 15 min. After the solution became clear, 2 mL of an aqueous solution containing 2 g KOH and 8.8 mg $Zn(CH_3COO)_2$ was added dropwise into the PVA solution and the stirring continued for 20 min. The charge and discharge polarization curves were recorded at 5 mV s^{-1} at room temperature. The cycling tests involved charge-discharge cycles of 10 min discharge followed by 10 min charge at a current density of 2 mA cm^{-2}.

Computational method

We performed plane-wave pseudopotential DFT calculations using the "Vienna ab initio Simulation Package" (VASP) code.[1, 2] The Perdew-Burke-Ernzerhof (PBE) functional with generalized gradient approximation (GGA) was employed for the exchange-correlation potentials, with the projector-augmented wave method used to describe the electron-ion interactions.[3, 4]

In the section on searching the best intermediate structure of $NiMo_xFe_{2(1-x)}O_4$, crystal structure predictions were carried out by using USPEX 10.5.0 code.[5-7] All calculations within the USPEX simulations were performed using the VASP code. A Hubbard correction of U = 5.5 eV and 3.0 eV was applied to Ni and Fe ions to correctly reproduce the magnetic order in $NiMo_xFe_yO_4$ system. In order to find the ground structure with proper magnetic order of this system, the probabilities of generating non-magnetic, low-spin ferromagnetic, high-spin ferromagnetic, low-spin antiferromagnetic, high-spin antiferromagnetic structures are all 20%. For the final optimization and subsequent self-consistent static calculations among the USPEX run, the used energy cutoff is 500 eV and density of k-points in the first Brillouin zone is $0.03 \times 2\pi$ Å^{-1} and $0.02 \times 2\pi$ Å^{-1} for all studied structures.

In the section on calculating OER pathway, the atomic structures are relaxed until the maximum force on each atom is less than 0.02 eV Å^{-1}, and an energy cutoff of 500 eV is used. A vacuum space

of ~20 Å along the z-direction is used to separate the interaction between the neighboring slabs. The bulk α-phase $NiMoO_4$ belongs to the space group C2/m with the following DFT calculated unit cell parameters: a = 9.5498 Å, b = 8.7215 Å, c = 7.6793 Å, β = 114.142°. The atomic structure of $NiMoO_4$-NC was modelled by the (110) surface of α-phase $NiMoO_4$, and the Brillouin zone is sampled by using a Monkhorst-Pack mesh of 3×2×1. The $NiMoO_4$-Fe-5th model was constructed by replacing one Mo atom on the $NiMoO_4$ (110) surface with two Fe atom, and the Brillouin zone was also sampled by using a Monkhorst-Pack mesh of 3×2×1. The bulk $NiFe_2O_4$ belongs to the in space group $Fd\bar{3}m$ with the following DFT calculated unit cell parameters: $a = b = c = 8.0485$ Å and $\alpha = \beta = \gamma = 90°$. The (100) surface of $NiFe_2O_4$ was chosen to study the four-electron process, and the Brillouin zone was sampled by using a Monkhorst-Pack mesh of 3×3×1.

The OER involves the following steps:

$$* + OH^- \rightarrow *OH + e^- \quad (1)$$

$$*OH + OH^- \rightarrow *O + H_2O + e^- \quad (2)$$

$$*O + OH^- \rightarrow *OOH + e^- \quad (3)$$

$$*OOH + OH^- \rightarrow * + O_2(g) + H_2O + e^- \quad (4)$$

where * represents the prefered adsorption site for intermediates. For each step of OER, the reaction free energy ΔG is defined as the difference in free energy of the initial and final states as calculated by the following equation:

$$\Delta G = \Delta E + \Delta ZPE - T\Delta S + \Delta G_U + \Delta G_{pH} \quad (5)$$

where ΔE is the total energy difference between reactants and products of the reactions, ΔZPE is the zero-point energy correction, ΔS is the vibrational entropy change at finite temperature T, $\Delta G_U = -eU$, where e is the elementary charge, U is the potential difference from the standard electrode potential (U = 1.23V), ΔG_{PH} represents the effect of PH value on the free energy.

The overpotential η of OER can be evaluated from the ΔG of each step as:

$$\eta_{OER} = \frac{max\{\Delta G_1, \Delta G_2, \Delta G_3, \Delta G_4\}}{e} \quad (6)$$

where $\Delta G_1, \Delta G_2, \Delta G_3,$ and ΔG_4 are the free energy reactions (1) to (4).

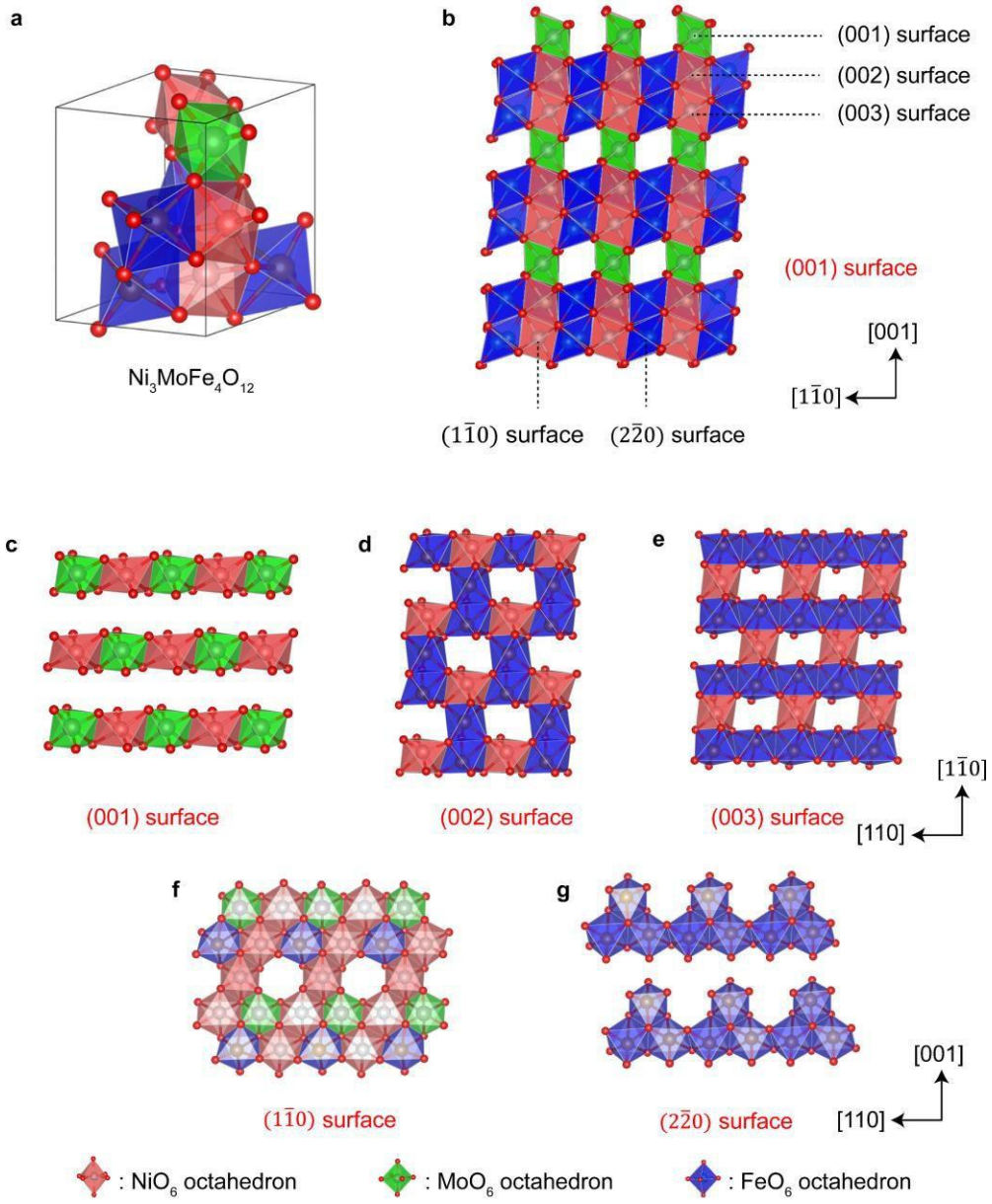

Figure S1. The structure with the lowest formation energy predicted by USPEX in the $NiMo_xFe_yO_4$ system. **(a)** Three-dimensional crystal structure of $Ni_3MoFe_4O_{12}$ unit cell with a = 5.48 Å, b = 5.61 Å, c = 7.67 Å, α = 92.94°, β = 98.02° and γ = 116.19°. **(b-g)** Two-dimensional crystal structure of $Ni_3MoFe_4O_{12}$ supercell. This structure is stacked in three layers of A_1-B_1-C_1 along [001] direction and in two layers of A_2-B_2 along [1$\bar{1}$0] direction, in which A_1-B_1-C_1 is (110), (001), (002) surface and A_2-B_2 is (1$\bar{1}$0), (2$\bar{2}$0) surface.

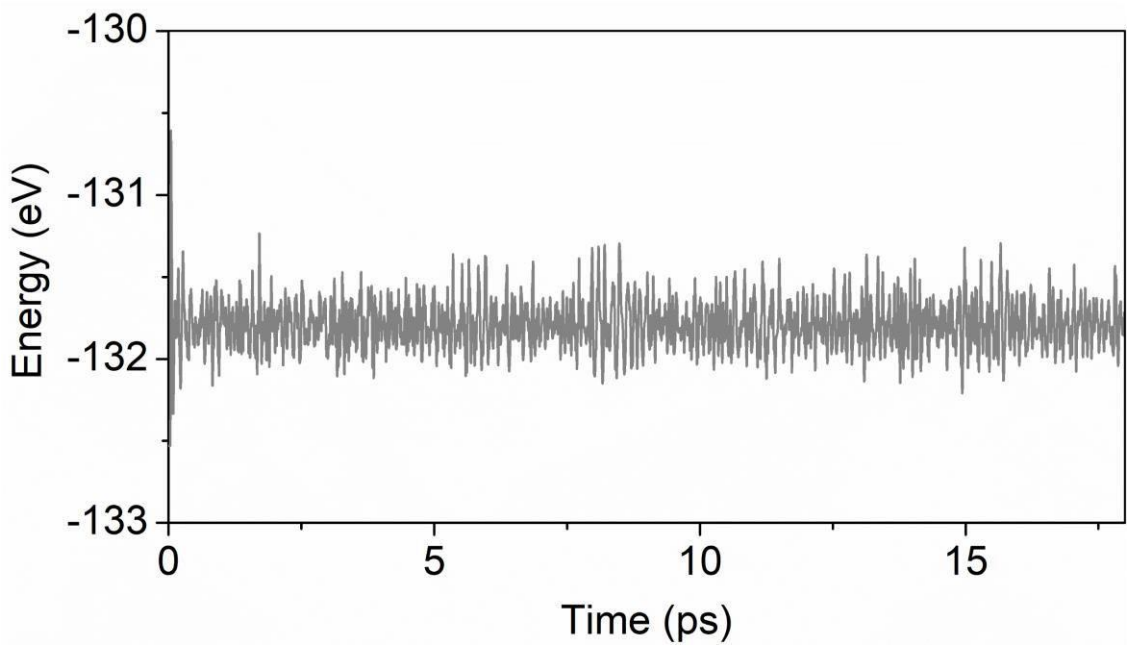

Figure S2. AIMD energy profile of $Ni_3MoFe_4O_{12}$ calculated by VASP code.

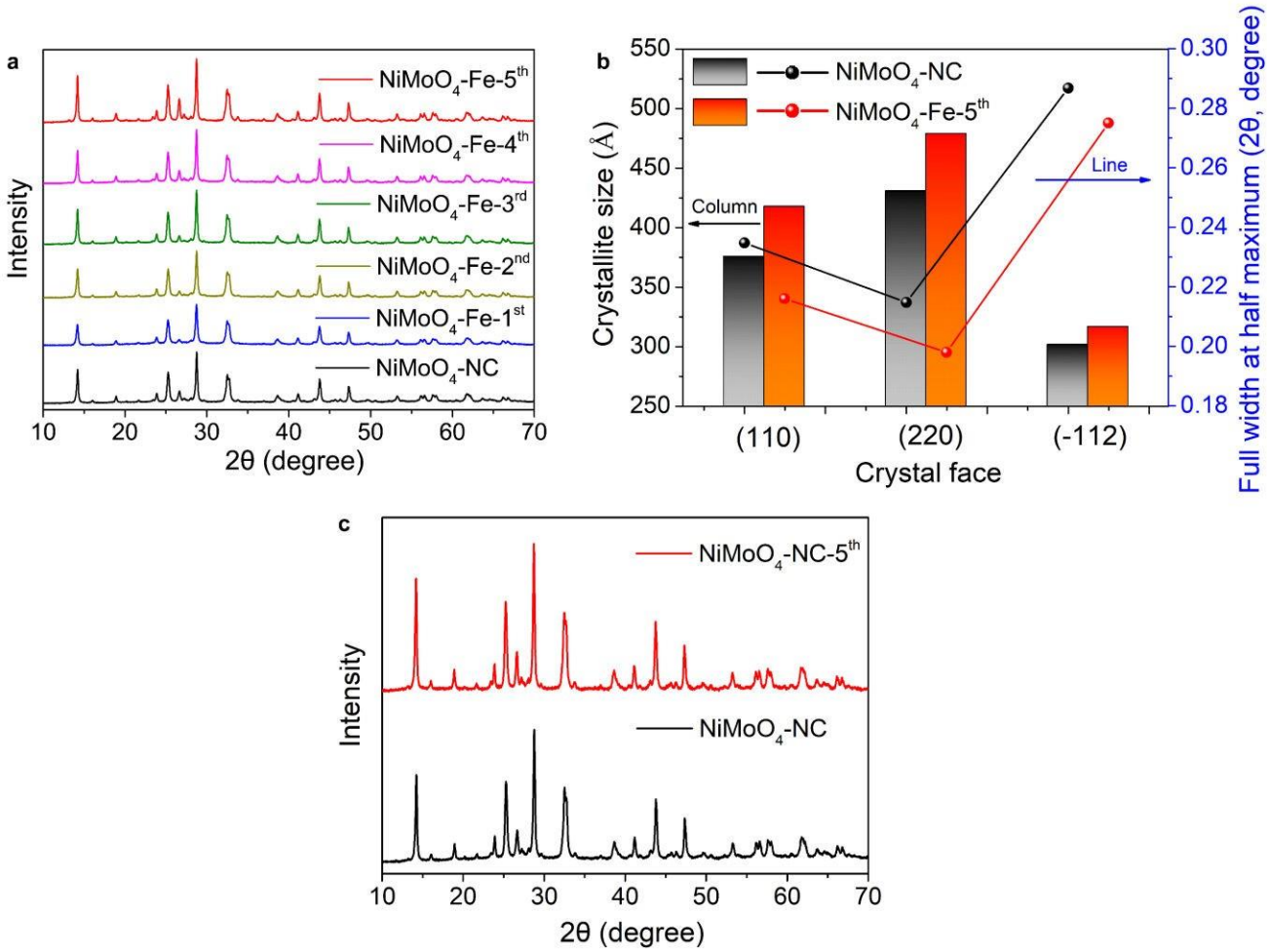

Figure S3. (a) XRD patterns for $NiMoO_4$-NC and $NiMoO_4$ catalysts multiple quenched in $Fe(NO_3)_3$ solution. **(b)** Full width at half maximum and crystallite size of different crystal faces obtained from XRD date. (c) XRD patterns for $NiMoO_4$-NC and $NiMoO_4$-NC-5^{th} (Repeat calcining five times under natural cooling).

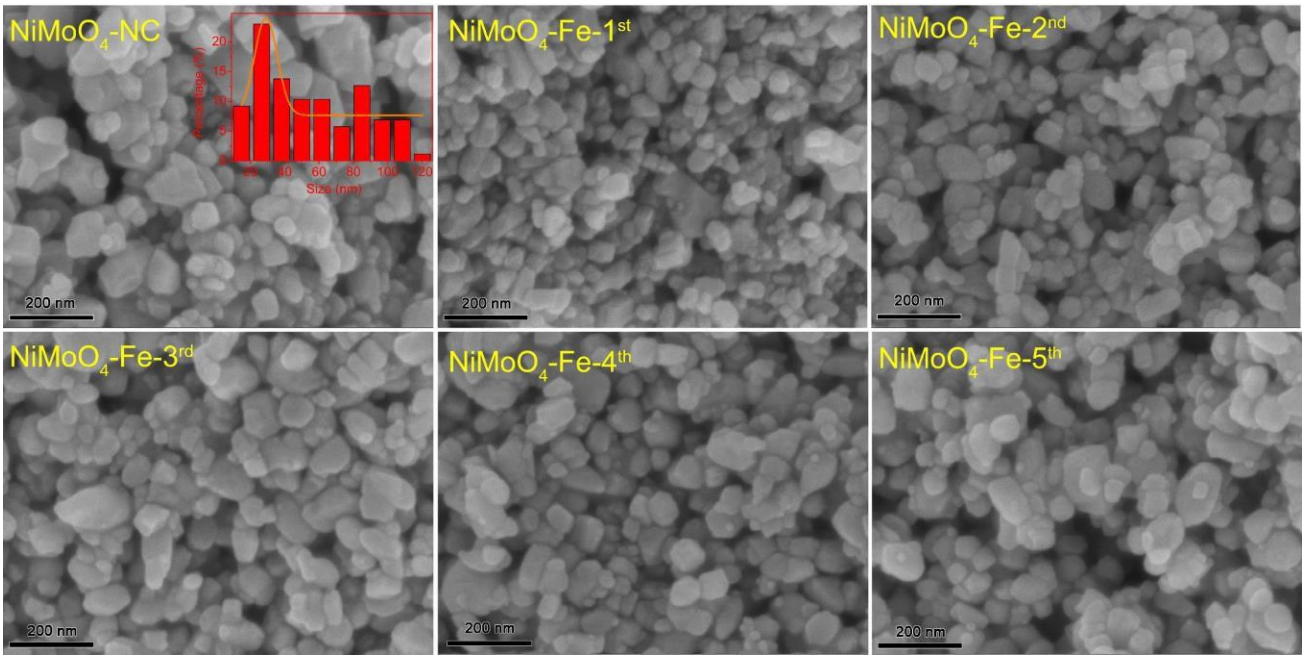

Figure S4. SEM images of $NiMoO_4$ catalysts multiple quenched in $Fe(NO_3)_3$ solution, compared with $NiMoO_4$-NC obtained by natural cooling (NC).

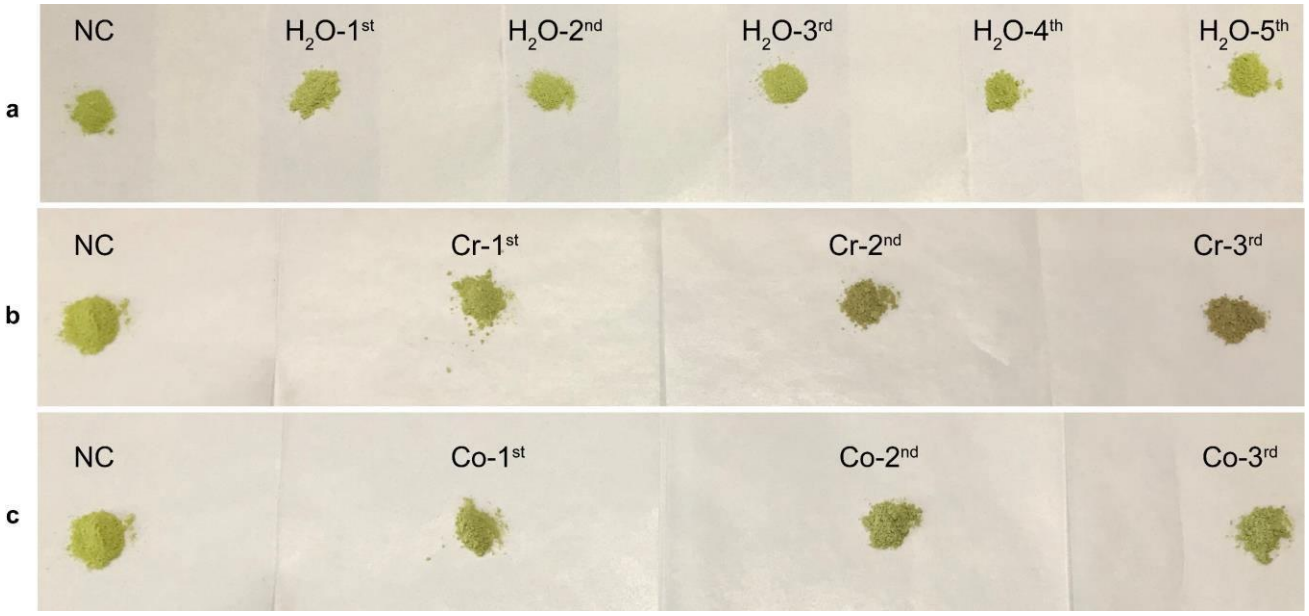

Figure S5. Digital photographs of $NiMoO_4$ catalysts multiple quenched in **(a)** H_2O, **(b)** 1 M $Cr(NO_3)_3$ or **(c)** 1 M $Co(NO_3)_2$ solutions. The $NiMoO_4$ catalyst prepared by natural cooling (NC) is also shown.

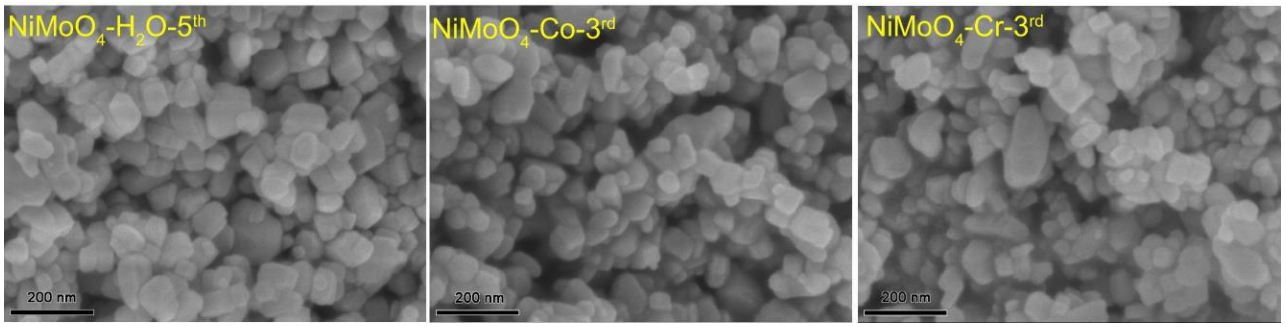

Figure S6. SEM images of $NiMoO_4$ catalysts multiple quenched in H_2O, $Co(NO_3)_2$ or $Cr(NO_3)_3$ solution.

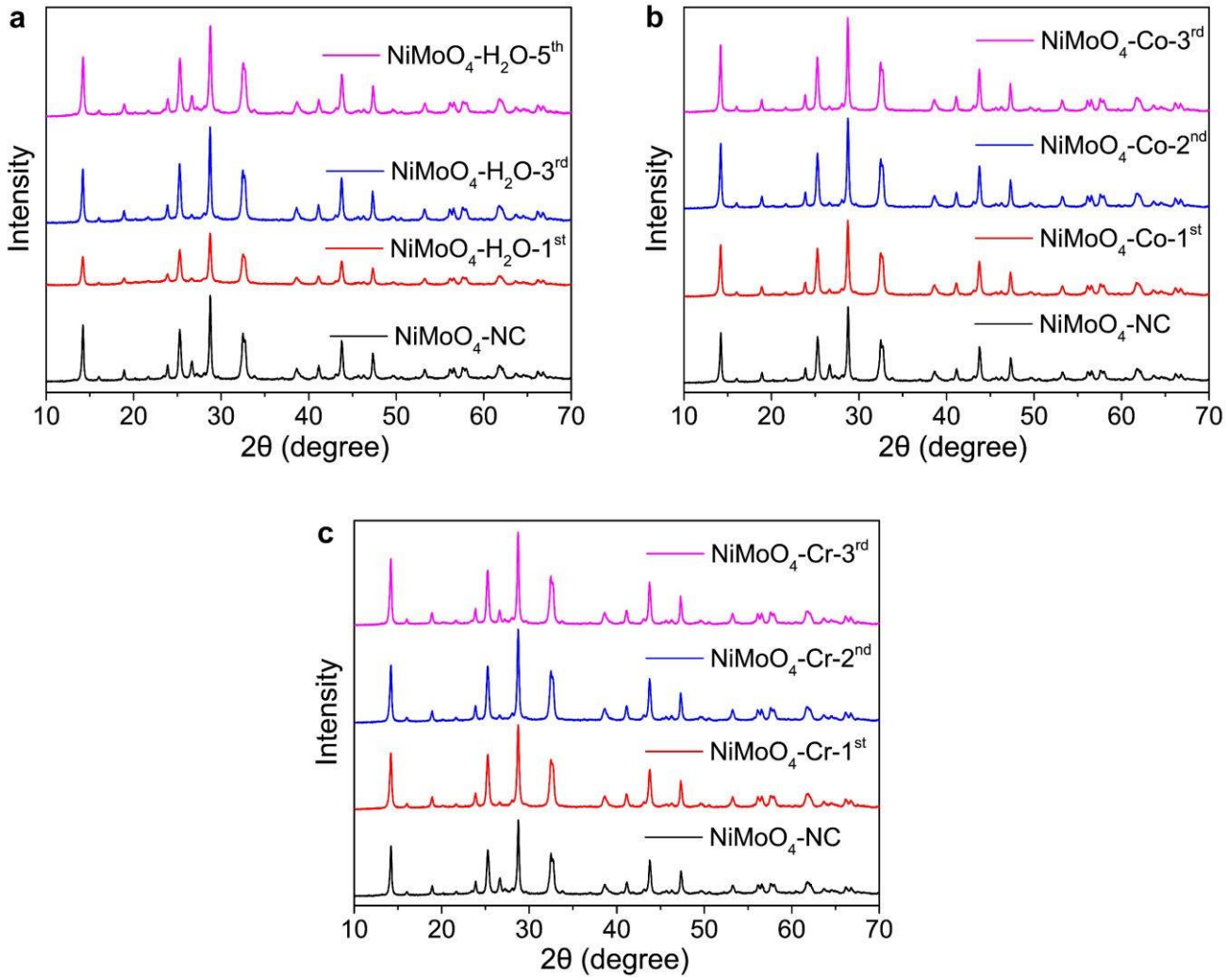

Figure S7. XRD patterns for $NiMoO_4$ catalysts multiple quenched in **(a)** H_2O, **(b)** $Co(NO_3)_2$ and **(c)** $Cr(NO_3)_3$ solution.

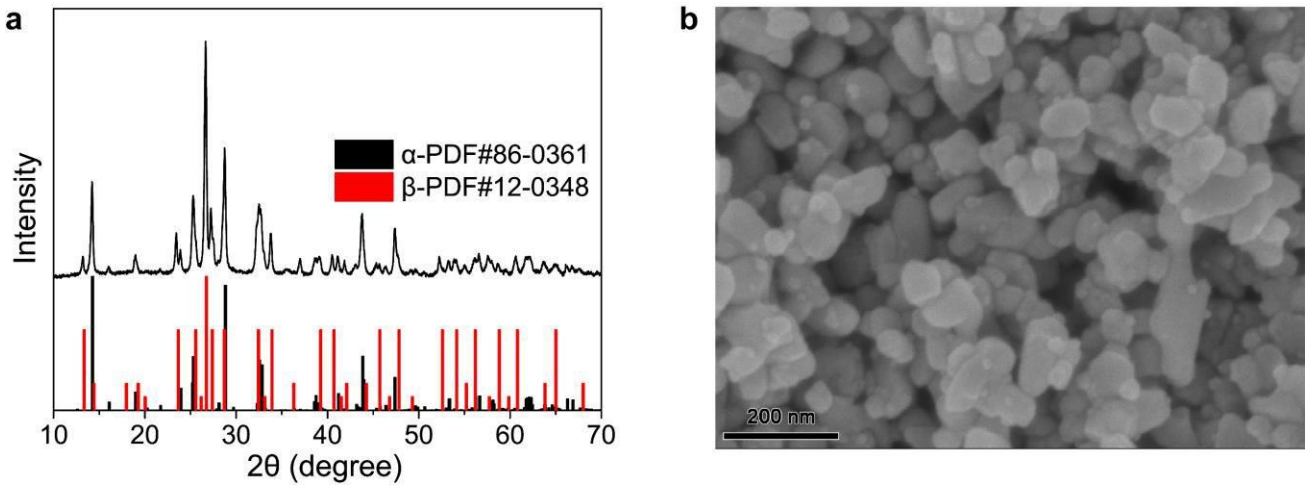

Figure S8. (a) XRD patterns and **(b)** SEM images for the Fe doped $NiMoO_4$-Fe-NC catalyst (natural cooling).

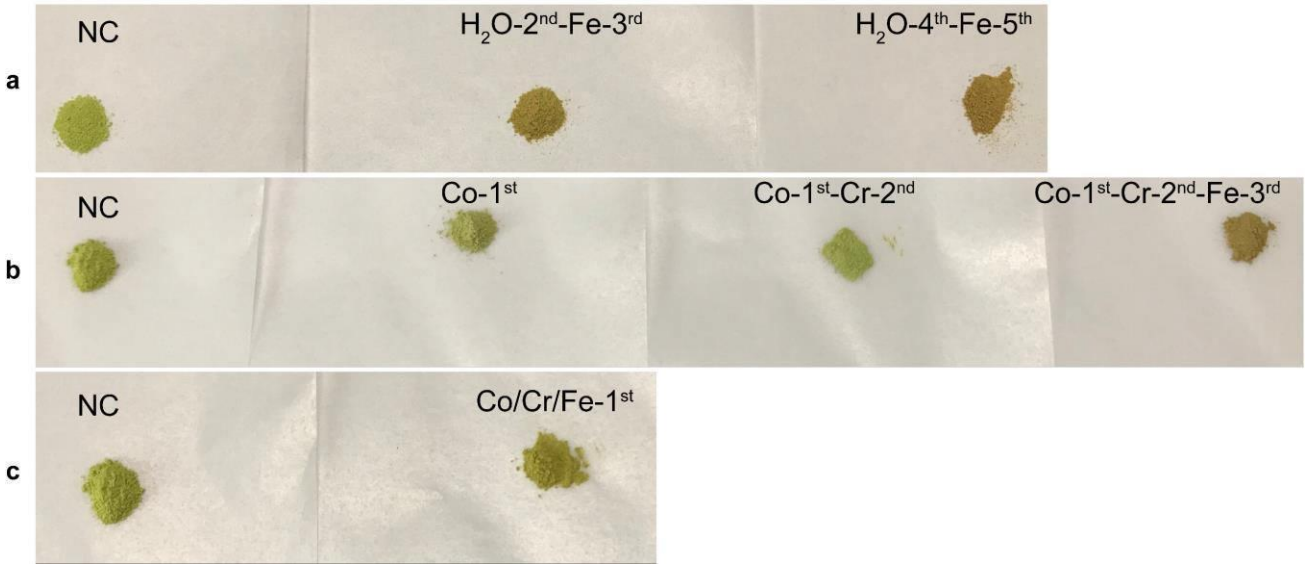

Figure S9. Digital photographs of **(a)** $NiMoO_4$ catalysts pre-quenched in water for 2 or 4 times and then quenched in 1 M $Fe(NO_3)_3$ solution. **(b)** $NiMoO_4$ catalysts pre-quenched successively in 1 M $Co(NO_3)_2$, 1 M $Cr(NO_3)_3$ solution, and finally quenched in 1 M $Fe(NO_3)_3$ solution. **(c)** $NiMoO_4$ catalysts quenched once in mixed solution of 1 M $Co(NO_3)_2$, 1 M $Cr(NO_3)_3$ and 1 M $Fe(NO_3)_3$. $NiMoO_4$ prepared by natural cooling (NC) is also shown for comparison.

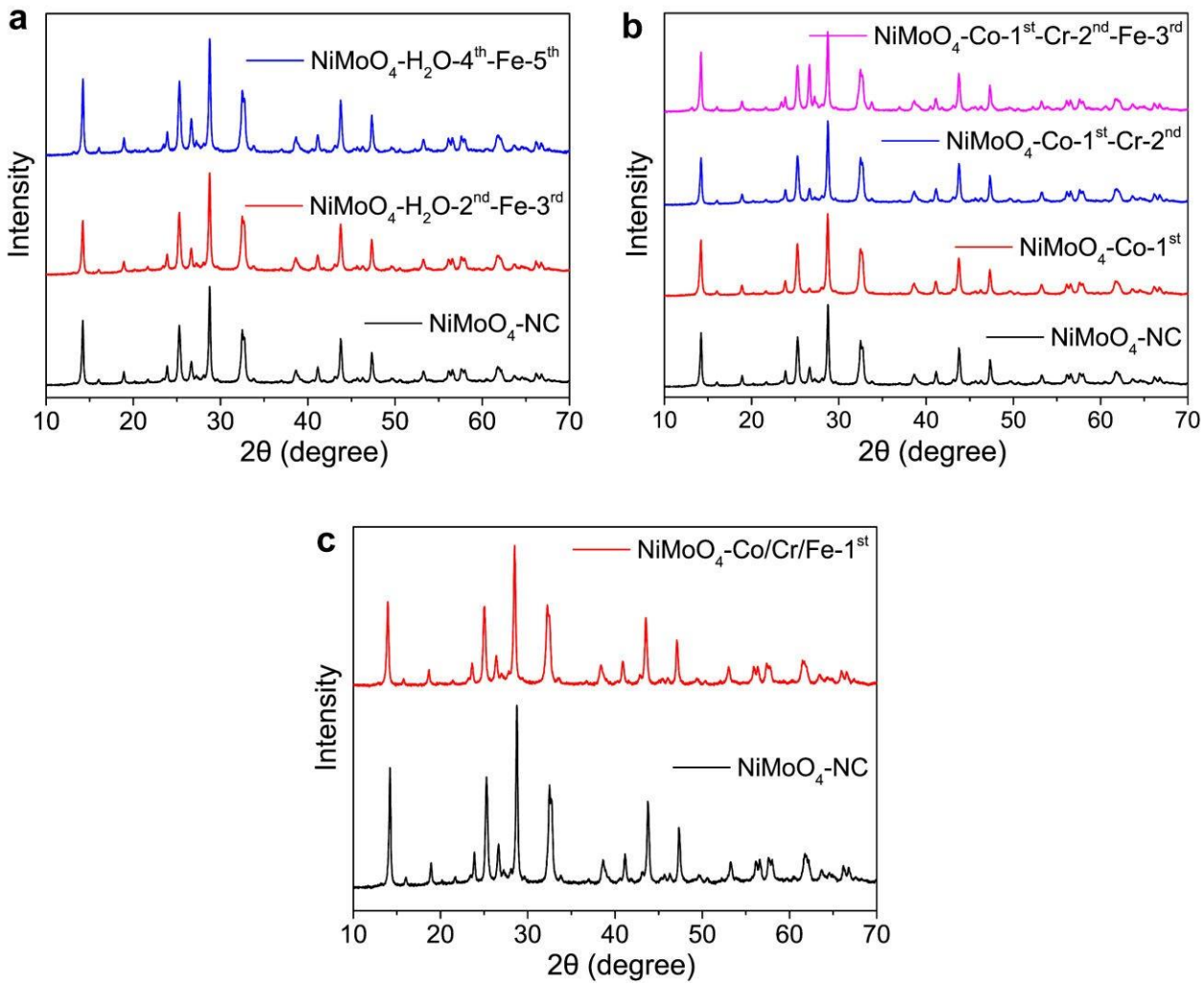

Figure S10. (a) XRD patterns for $NiMoO_4$ catalysts pre-quenched in water and then quenched in $Fe(NO_3)_3$ solution; **(b)** XRD patterns for $NiMoO_4$ catalysts pre-quenched successively in $Co(NO_3)_2$ solution and $Cr(NO_3)_3$ solution, and finally quenched in $Fe(NO_3)_3$ solution; **(c)** XRD patterns for $NiMoO_4$ catalysts quenched once in a mixed solution of $Co(NO_3)_2$, $Cr(NO_3)_3$ and $Fe(NO_3)_3$, compared with $NiMoO_4$ prepared by natural cooling.

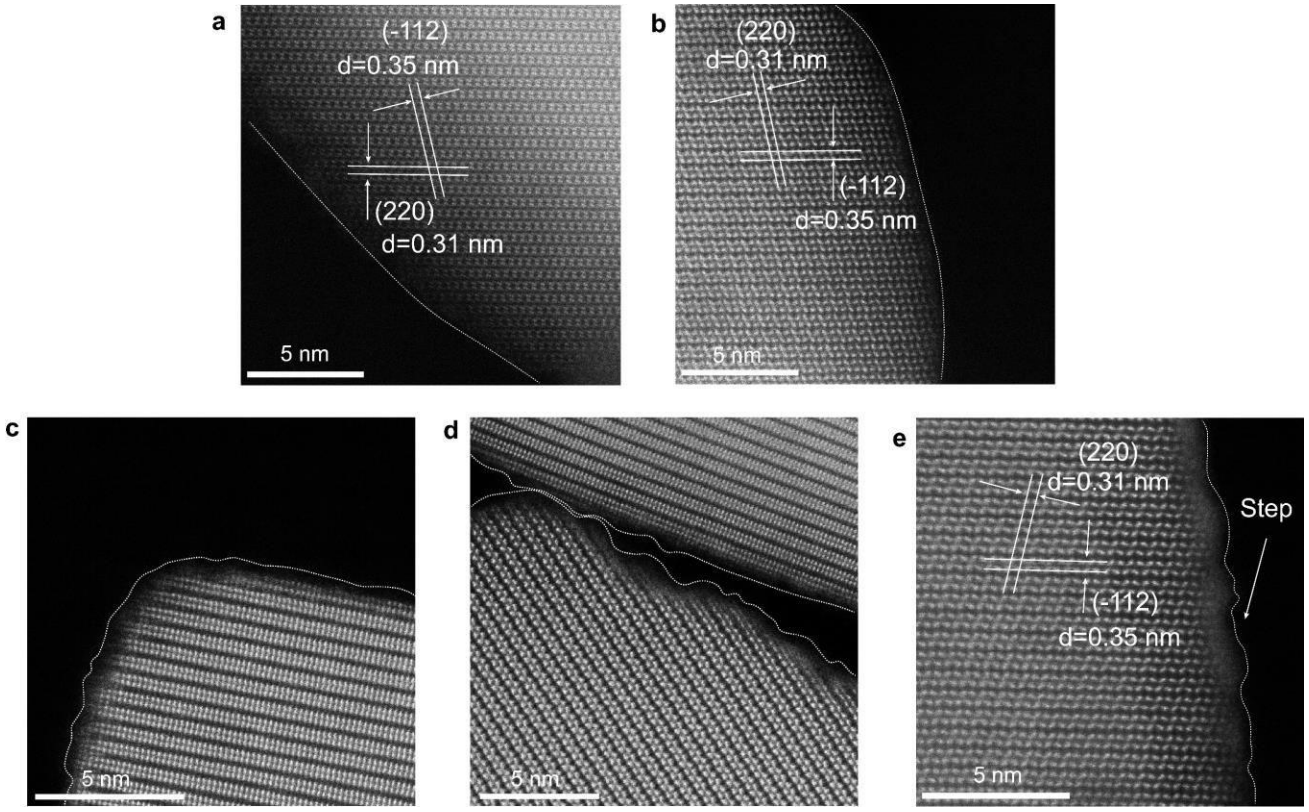

Figure S11. HAADF-STEM images of large particles **(a)** $NiMoO_4$-NC, **(b)** $NiMoO_4$-Fe-NC, **(c)** $NiMoO_4$-Fe-1st, **(d)** $NiMoO_4$-Fe-3rd, and **(e)** $NiMoO_4$-Fe-5th.

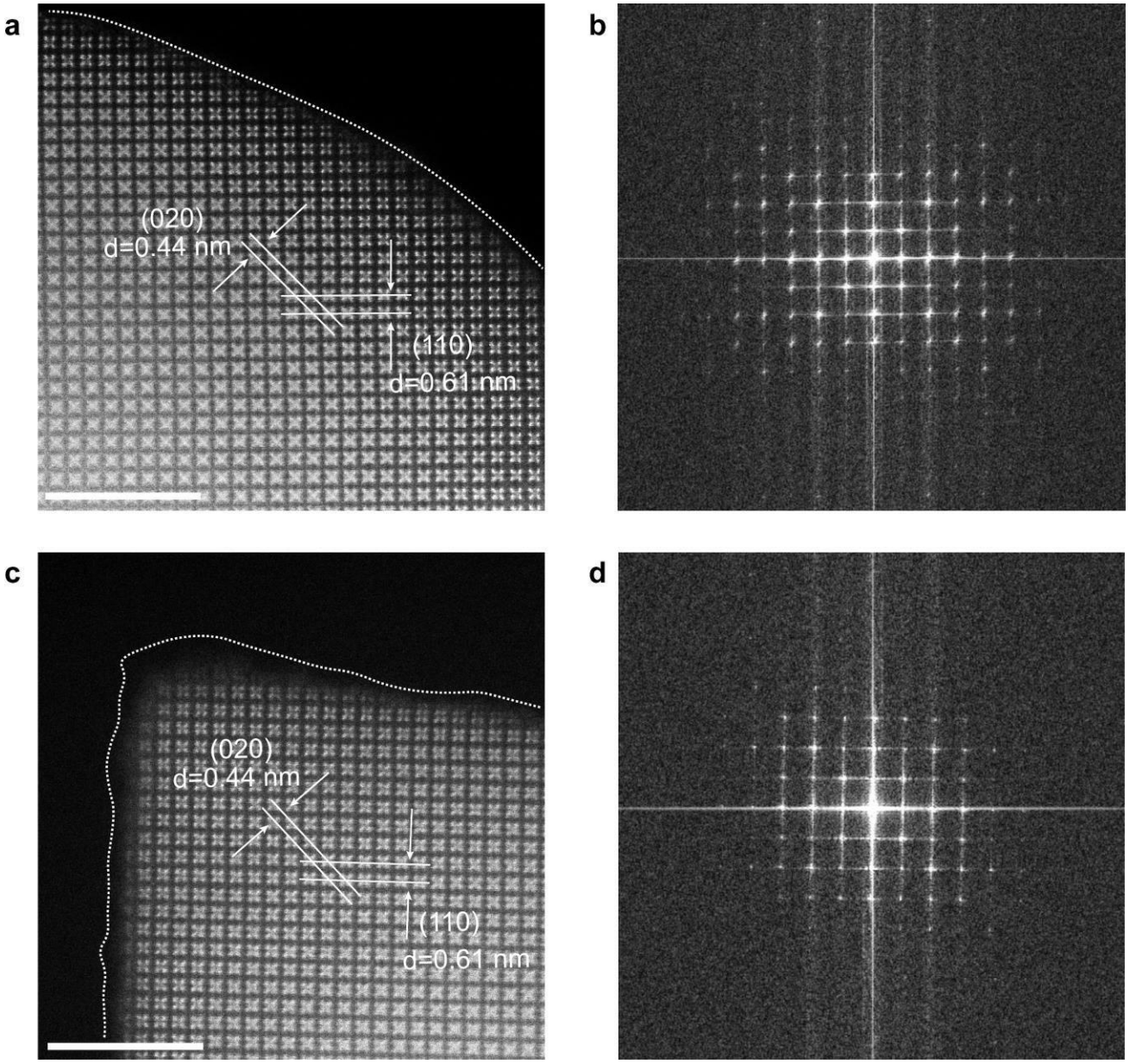

Figure S12. HAADF-STEM images of large particles **(a and b)** $NiMoO_4$-Fe-NC, and **(c and d)** $NiMoO_4$-Fe-5^{th}. The scale bar is 5 nm. Images are viewed down the [001] zone axis.

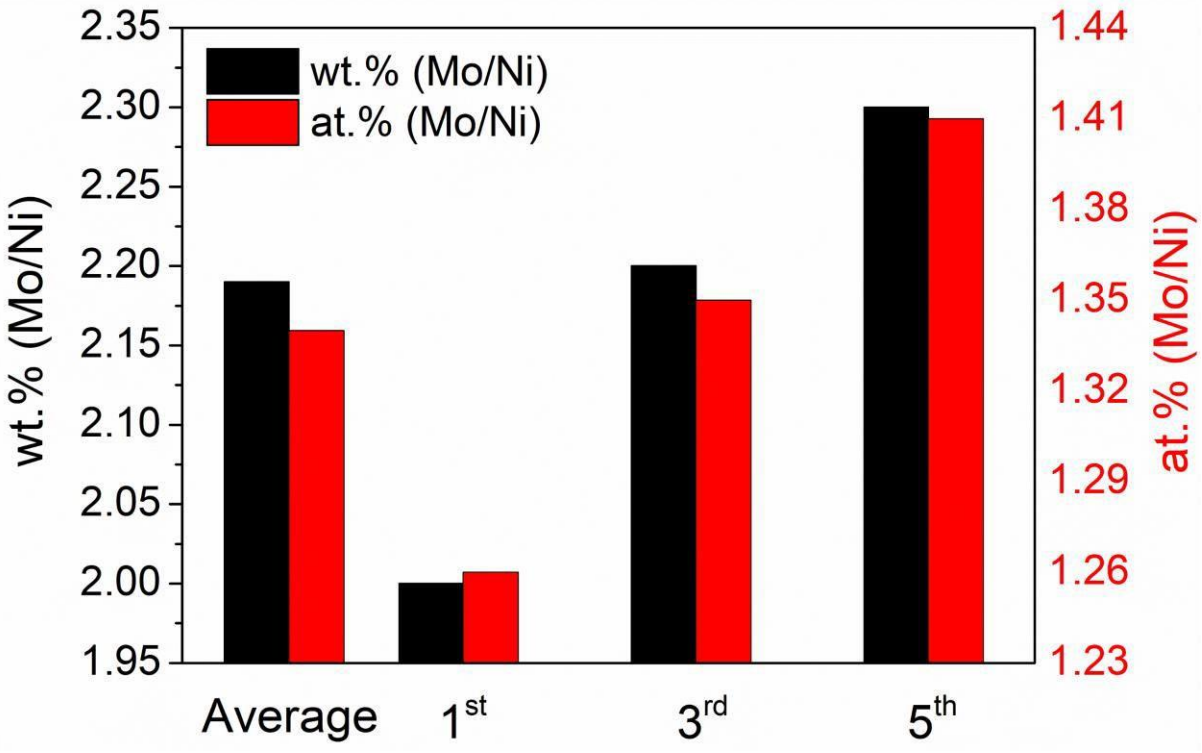

Figure S13. The metal contents in the $Fe(NO_3)_3$ quenching solution after different quenching cycles determined by ICP-MS. After $NiMoO_4$ was quenched in $Fe(NO_3)_3$ solution, the suspension was filtered to remove $NiMoO_4$ particles, and the obtained $Fe(NO_3)_3$ solution was taken for ICP analysis.

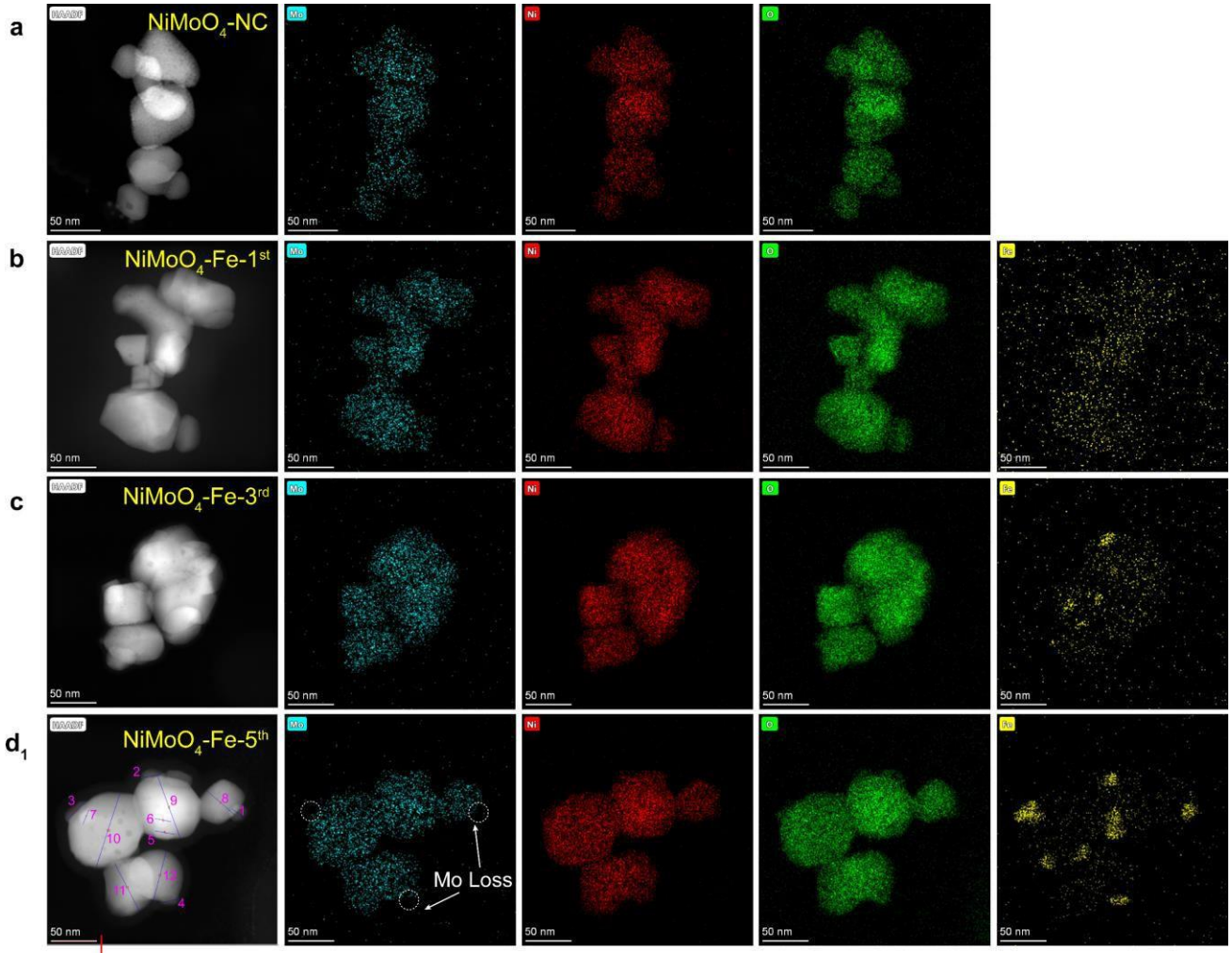

No.	1	2	3	4	5	6	7	8	9	10	11	12
Size (nm)	17	21	27	20	22	18	18	41	71	84	60	57
Change	$NiMoO_4 \rightarrow NiFe_2O_4$							Fe doped $NiMoO_4$				

No.	1	2	3	4	5	6	7	8	9	10	11	12
Size (nm)	19	12	17	27	22	11	32	72	78	74	74	67
Change	$NiMoO_4 \rightarrow NiFe_2O_4$						Fe doped $NiMoO_4$					

Figure S14. EDX elemental maps for **(a)** $NiMoO_4$-NC, **(b)** $NiMoO_4$-Fe-1st, **(c)** $NiMoO_4$-Fe-3rd and **(d_1 and d_2)** $NiMoO_4$-Fe-5th. Tables shows particle sizes for $NiMoO_4$-Fe-5th. The in-situ transition from $NiMoO_4$ to $NiFe_2O_4$ was mainly seen in small particles of size less than 27 nm.

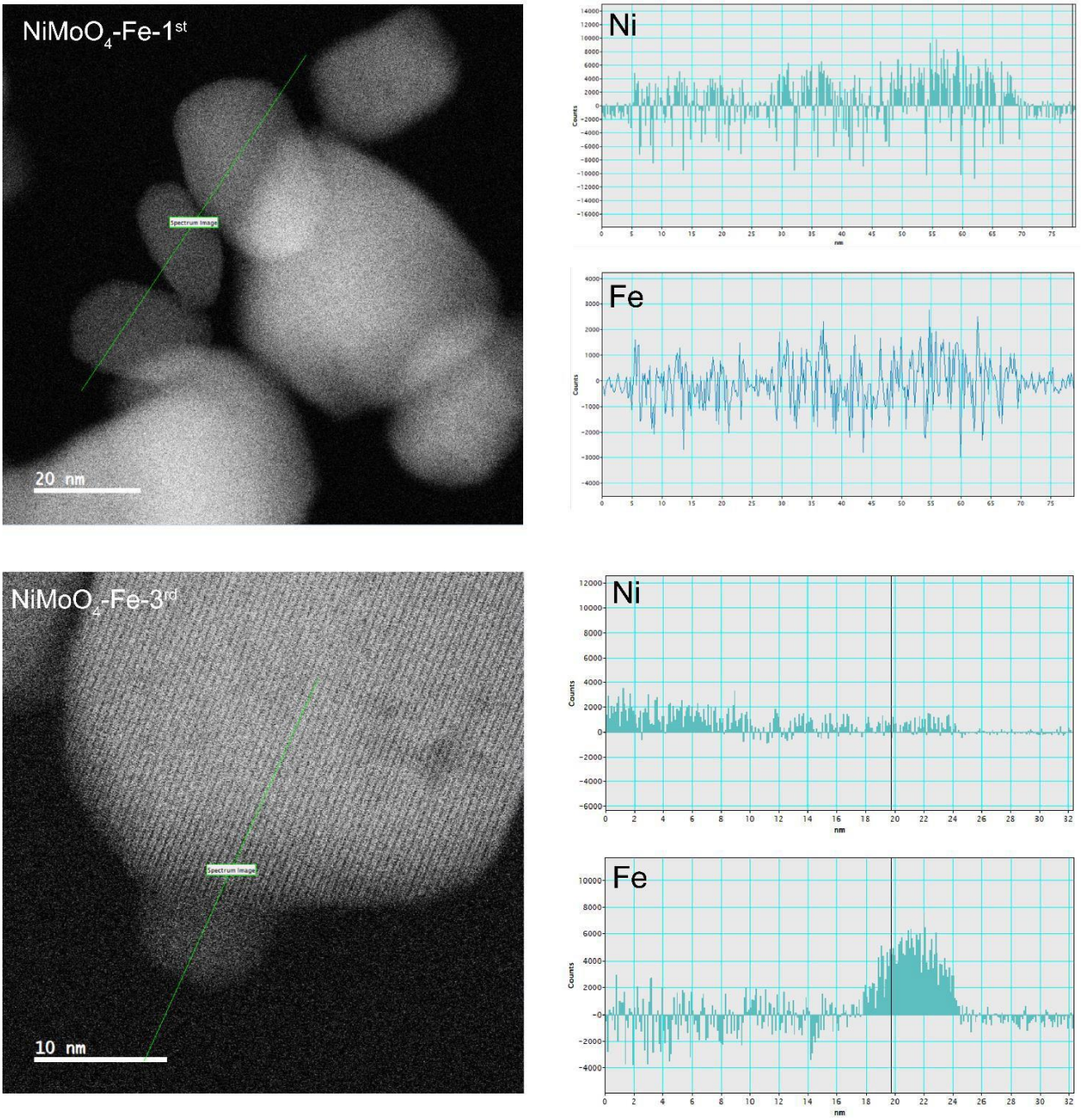

Figure S15. EELS linear scans for $NiMoO_4$-Fe-1st and $NiMoO_4$-Fe-3rd.

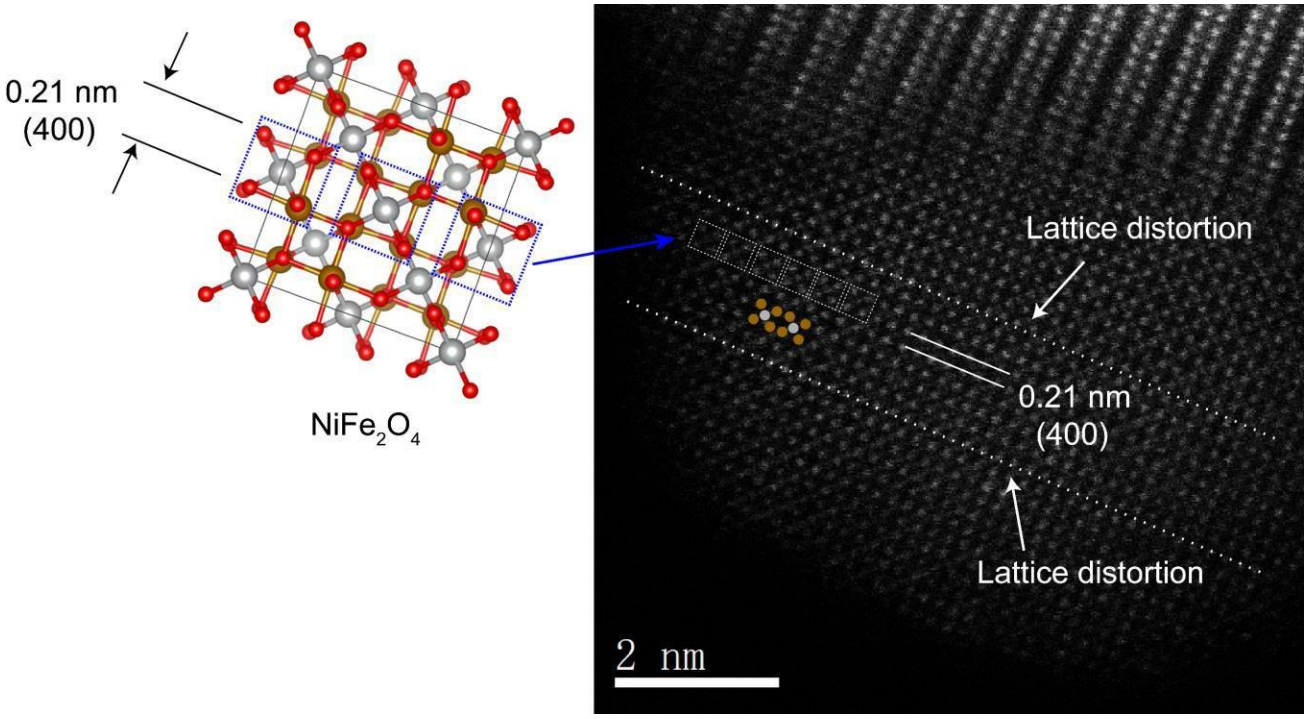

Figure S16. HAADF-STEM images of $NiMoO_4$-Fe-3rd.

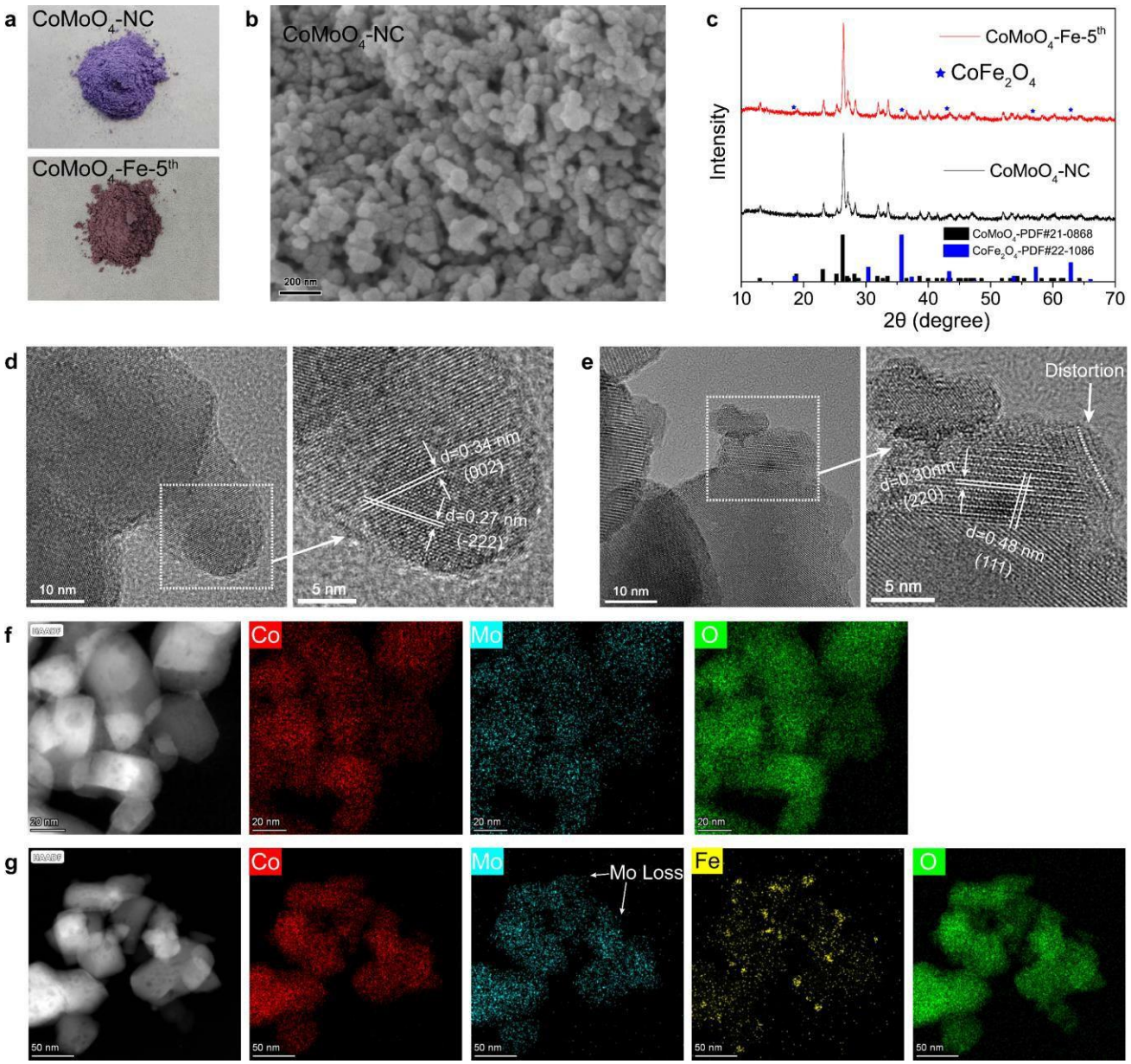

Figure S17. (a) Digital photographs of $CoMoO_4$-NC and $CoMoO_4$-Fe-5^{th} catalysts; **(b)** SEM images for the $CoMoO_4$-NC catalyst; **(c)** XRD patterns for $CoMoO_4$-NC and $CoMoO_4$-Fe-5^{th} catalysts; TEM and EDX elemental map images of **(d and f)** $CoMoO_4$-NC and **(e and g)** $CoMoO_4$-Fe-5^{th} catalysts.

To verify the universality of multiple quenching-induced structural transformations to synthesize heterostructured catalyst, we synthesized purple $CoMoO_4$ nanoparticles with particle sizes of around 10-60 nm (Figure S17b), and also subjected them to multiple quenching in 1 M $Fe(NO_3)_3$ solution. The results show that the color of $CoMoO_4$ changes from purple to brown after five quenching (Figure S17a). Although the main structure of $CoMoO_4$ is still maintained, it contains a small amount of $CoFe_2O_4$ characteristic peaks for $CoMoO_4$-Fe-5^{th} catalysts (Figure S17c). High-resolution TEM shows that $CoMoO_4$-NC (naturally cooling) has an intact lattice surface (Figure S17d) and a uniform element distribution (Figure S17f). On the contrary, the surface of $CoMoO_4$-Fe-5^{th} has a lattice twisted structure and is exposed as the stepped surface, indicating that multiple quenching also has a strong regulatory effect on $CoMoO_4$. It is worth noting that the EDS element maps shows that quenching-induced Fe

doping also accumulates in the small particles accompanied by the loss of Mo for $CoMoO_4$-Fe-5th catalysts, indicating that $CoMoO_4$ transforms into CoFe oxide after five quenching. Based on the XRD spectrum, it can be concluded that multiple quenching also induces the structural transformation of $CoMoO_4$, forming a $CoMoO_4/CoFe_2O_4$ heterostructured catalyst, which is consistent with the results of $NiMoO_4$.

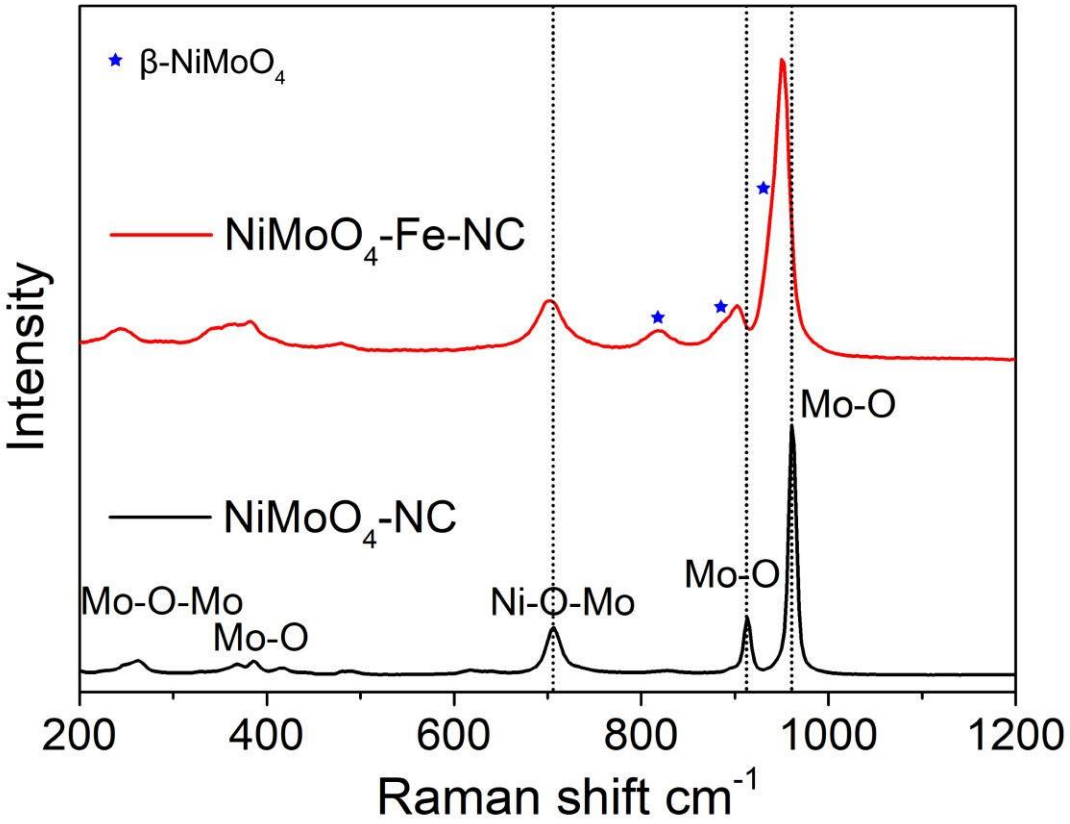

Figure S18. Raman spectra for $NiMoO_4$-Fe-NC and $NiMoO_4$-NC.

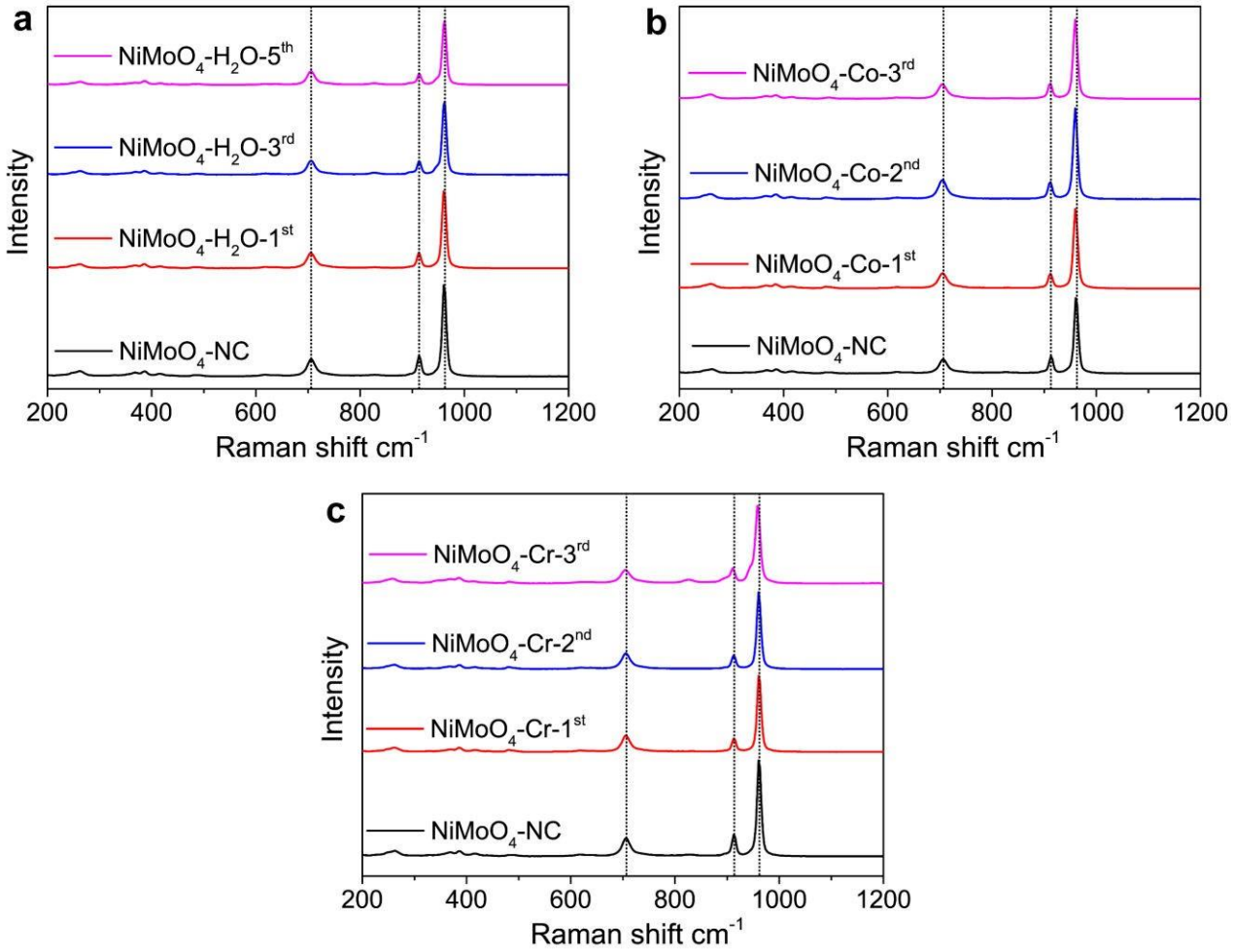

Figure S19. Raman spectra for $NiMoO_4$ catalysts multiple quenched in **(a)** H_2O, **(b)** $Co(NO_3)_2$ and **(c)** $Cr(NO_3)_3$ solutions, respectively.

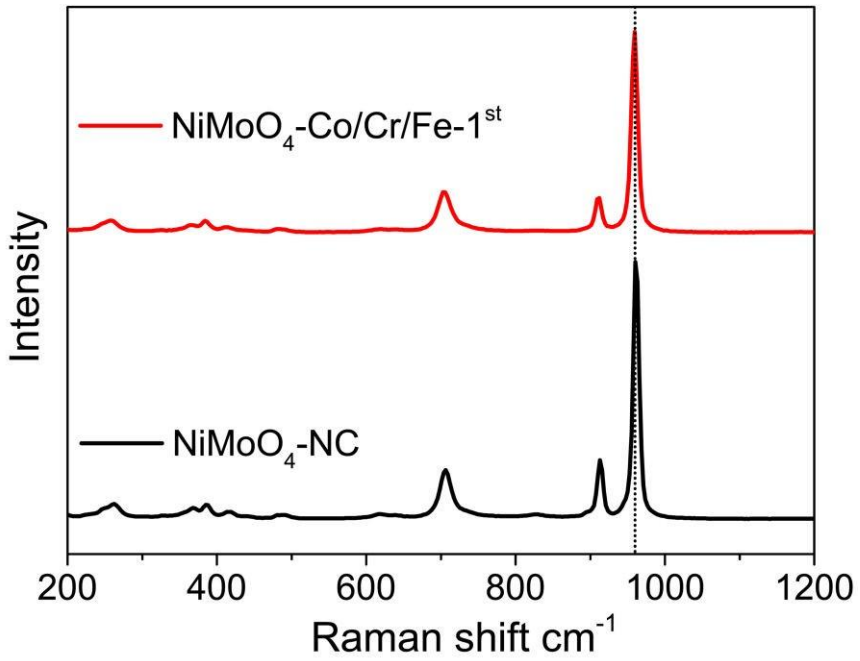

Figure S20. Raman spectra for $NiMoO_4$ catalysts quenched once in a mixed solution of $Co(NO_3)_2$, $Cr(NO_3)_3$ and $Fe(NO_3)_3$, compared with $NiMoO_4$ prepared by natural cooling.

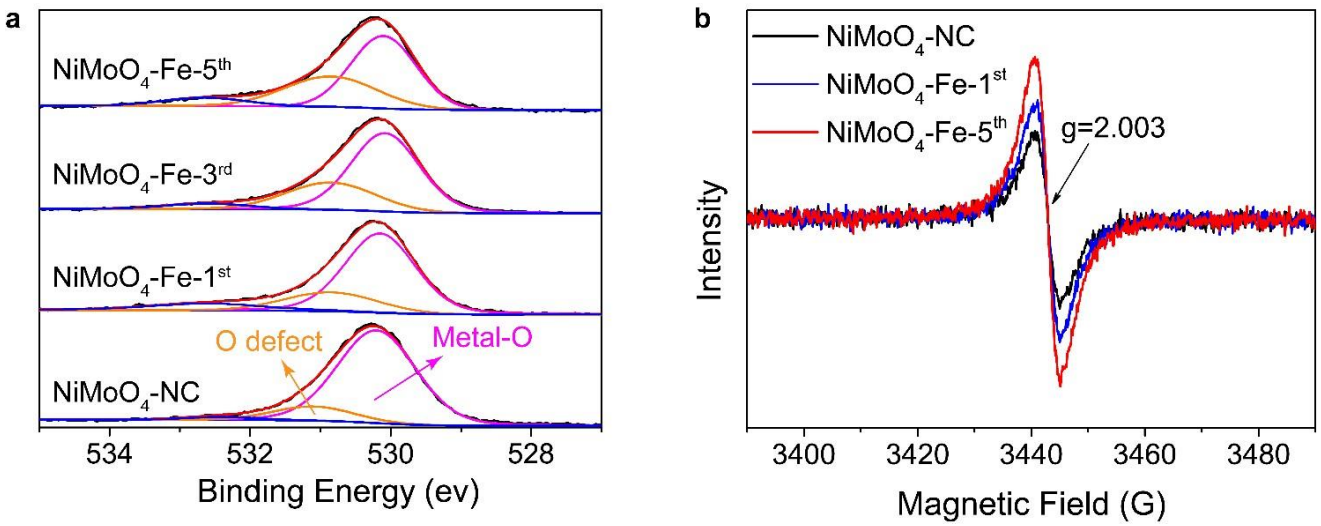

Figure S21. (a) O 1s XPS spectra for $NiMoO_4$-NC and selected $NiMoO_4$-Fe-X nanocatalysts; **(b)** EPR spectra of $NiMoO_4$-NC, $NiMoO_4$-Fe-1st and $NiMoO_4$-Fe-5th.

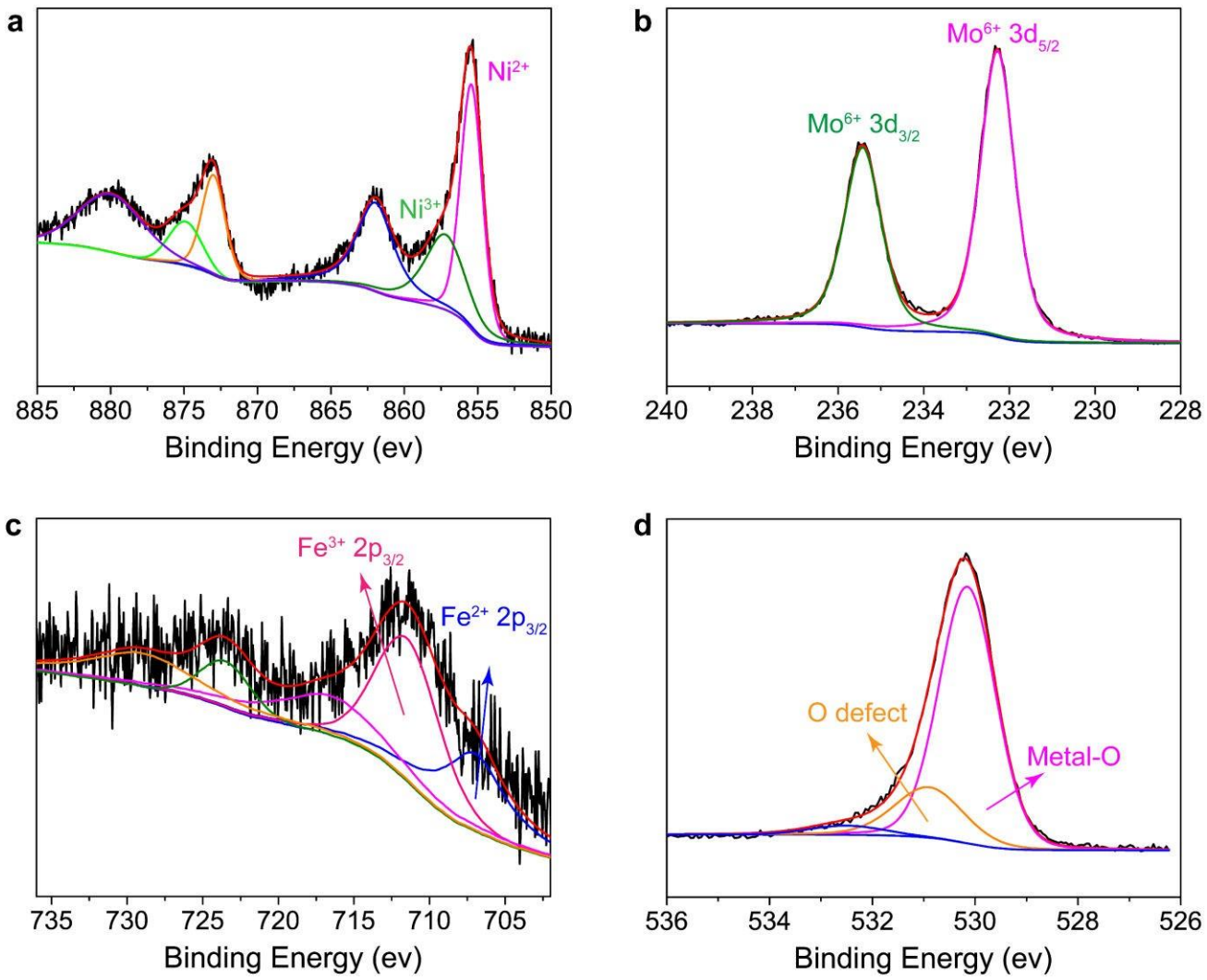

Figure S22. XPS spectra for the $NiMoO_4$-Fe-NC nanocatalyst: **(a)** Ni 2p, **(b)** Mo 3d, **(c)** Fe 2p and **(d)** O1s.

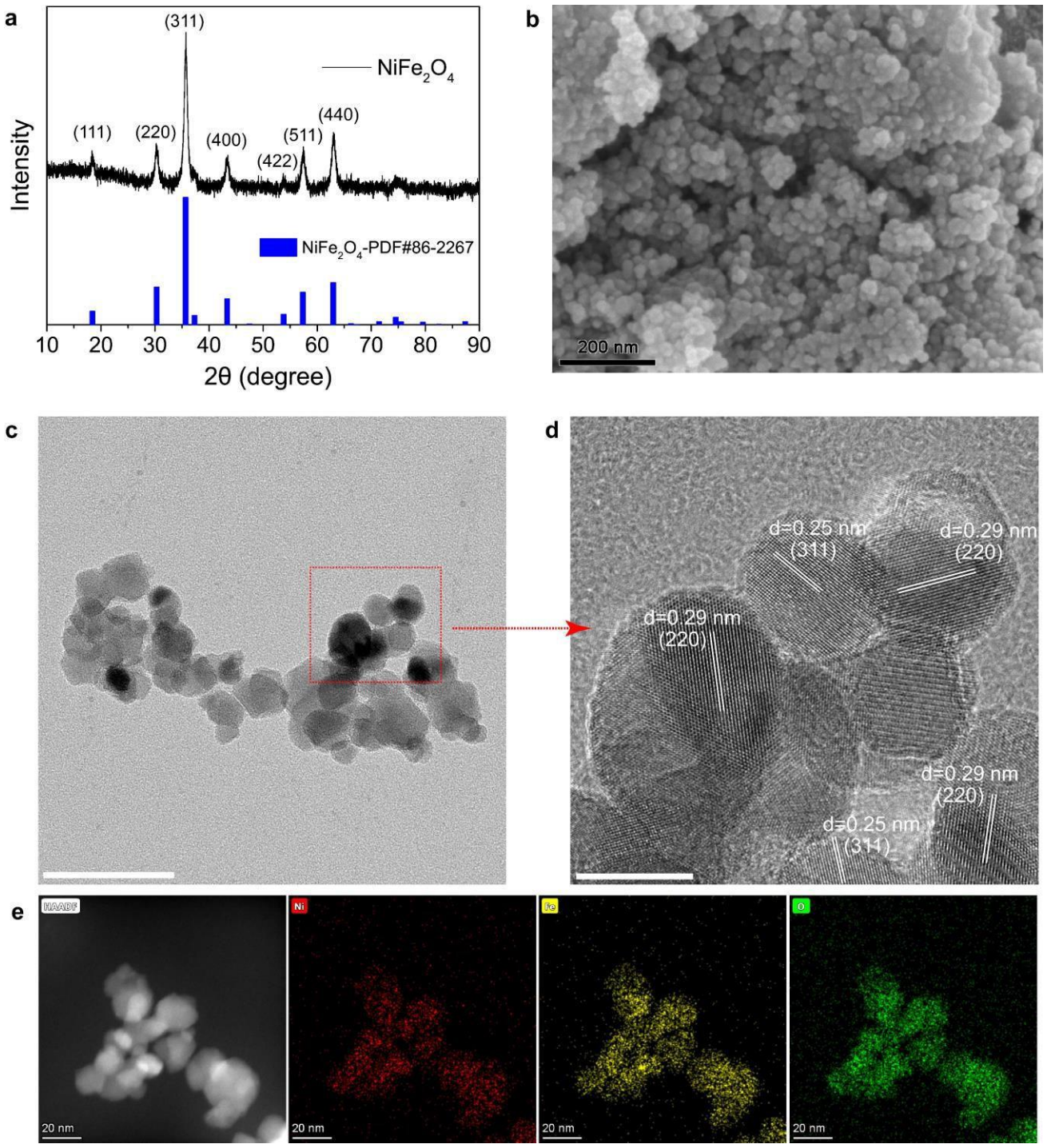

Figure S23. (a) XRD patterns and **(b)** SEM image for the $NiFe_2O_4$ catalyst. **(c and d)** High-resolution TEM images, and **(e)** EDX elemental maps for the $NiFe_2O_4$ catalyst. The scale bar is 50 nm for **(c)**, and 10 nm for **(d)**.

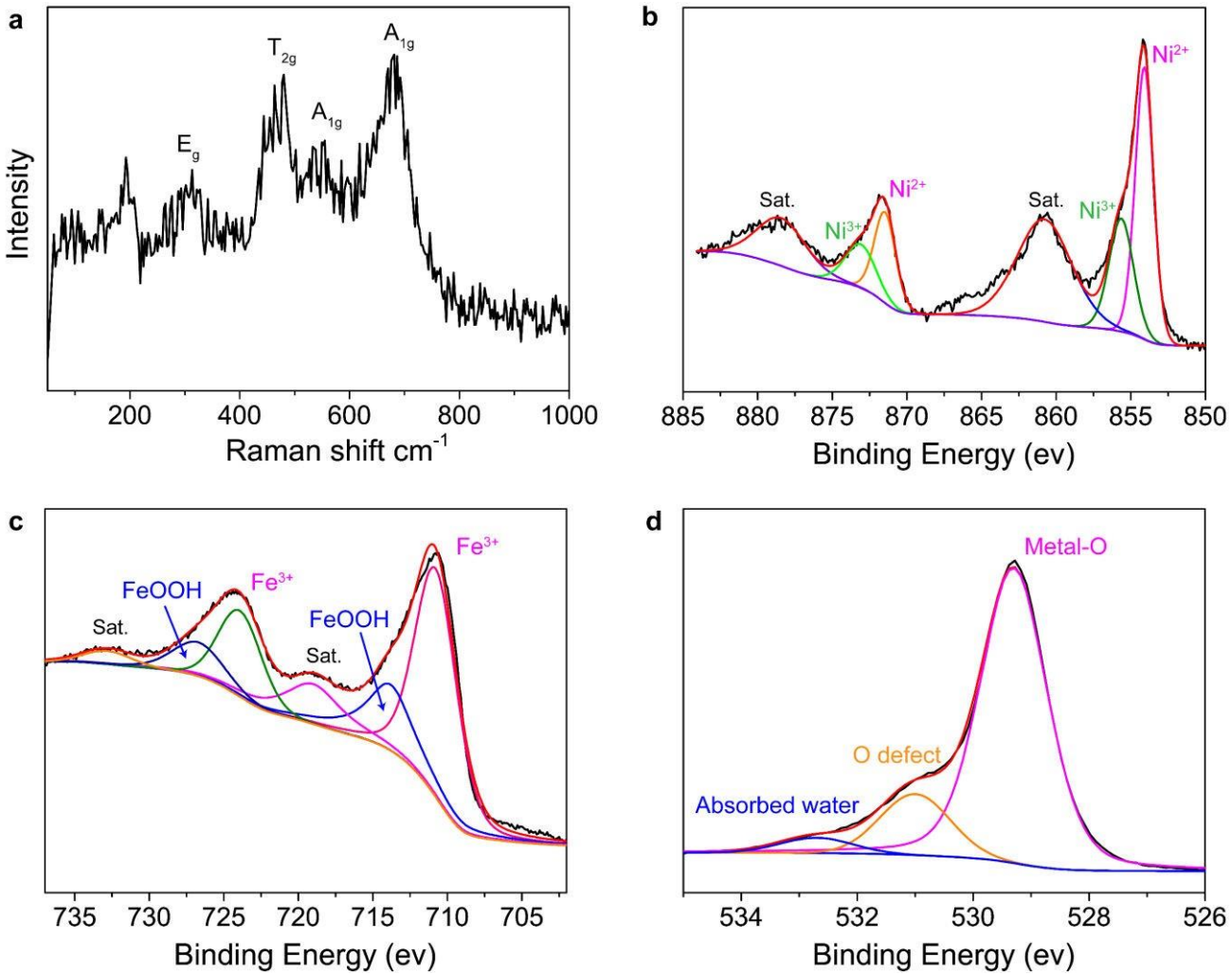

Figure S24. (a) Raman spectrum for the $NiFe_2O_4$ catalyst. XPS spectra for the $NiFe_2O_4$ catalyst: **(b)** Ni 2p, **(c)** Fe 2p and **(d)** O1s. The Fe 2p spectrum contains contributions from $NiFe_2O_4$ as the dominant species and surface Fe(Ni)OOH.

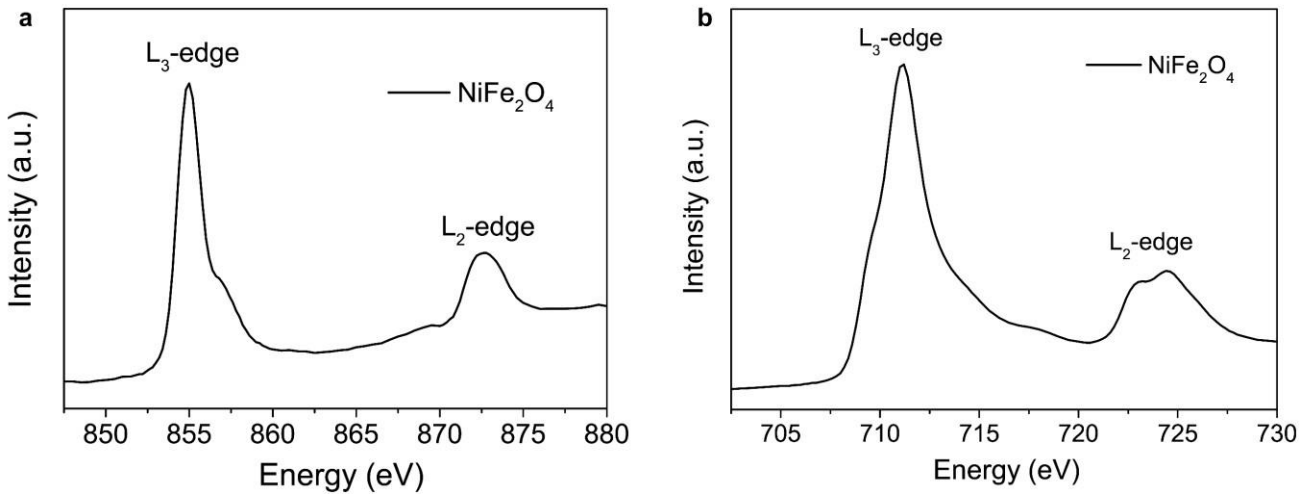

Figure S25. XAS spectra at the **(a)** Ni L-edge and **(b)** Fe L-edge spectra for the $NiFe_2O_4$ catalyst.

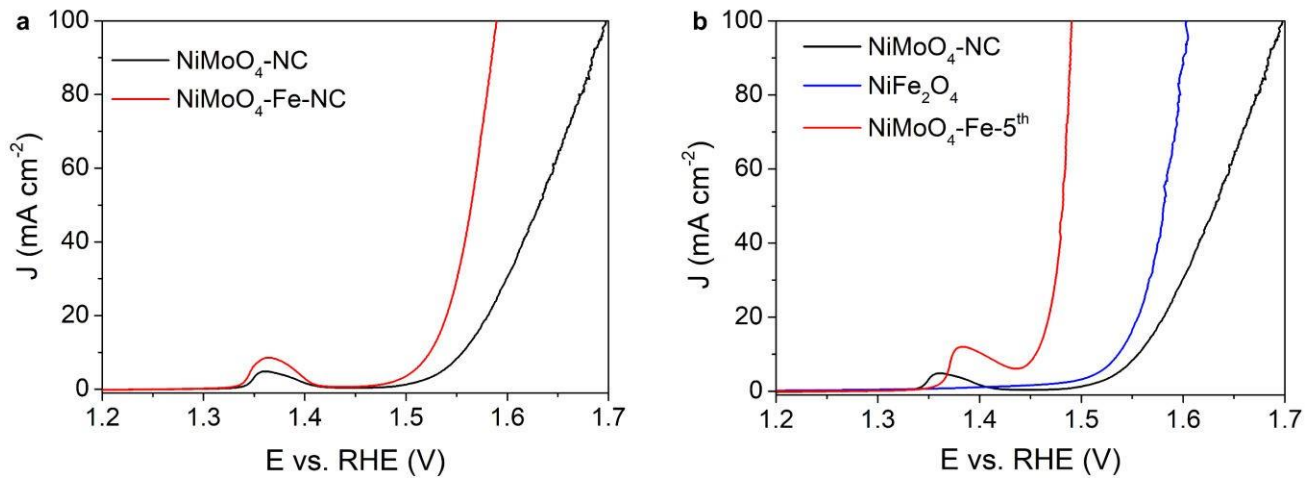

Figure S26. OER polarization curves in 1 M KOH solution for **(a)** $NiMoO_4$-Fe-NC compared with $NiMoO_4$-NC, and **(b)** $NiFe_2O_4$ compared with $NiMoO_4$-NC and $NiMoO_4$-5^{th}.

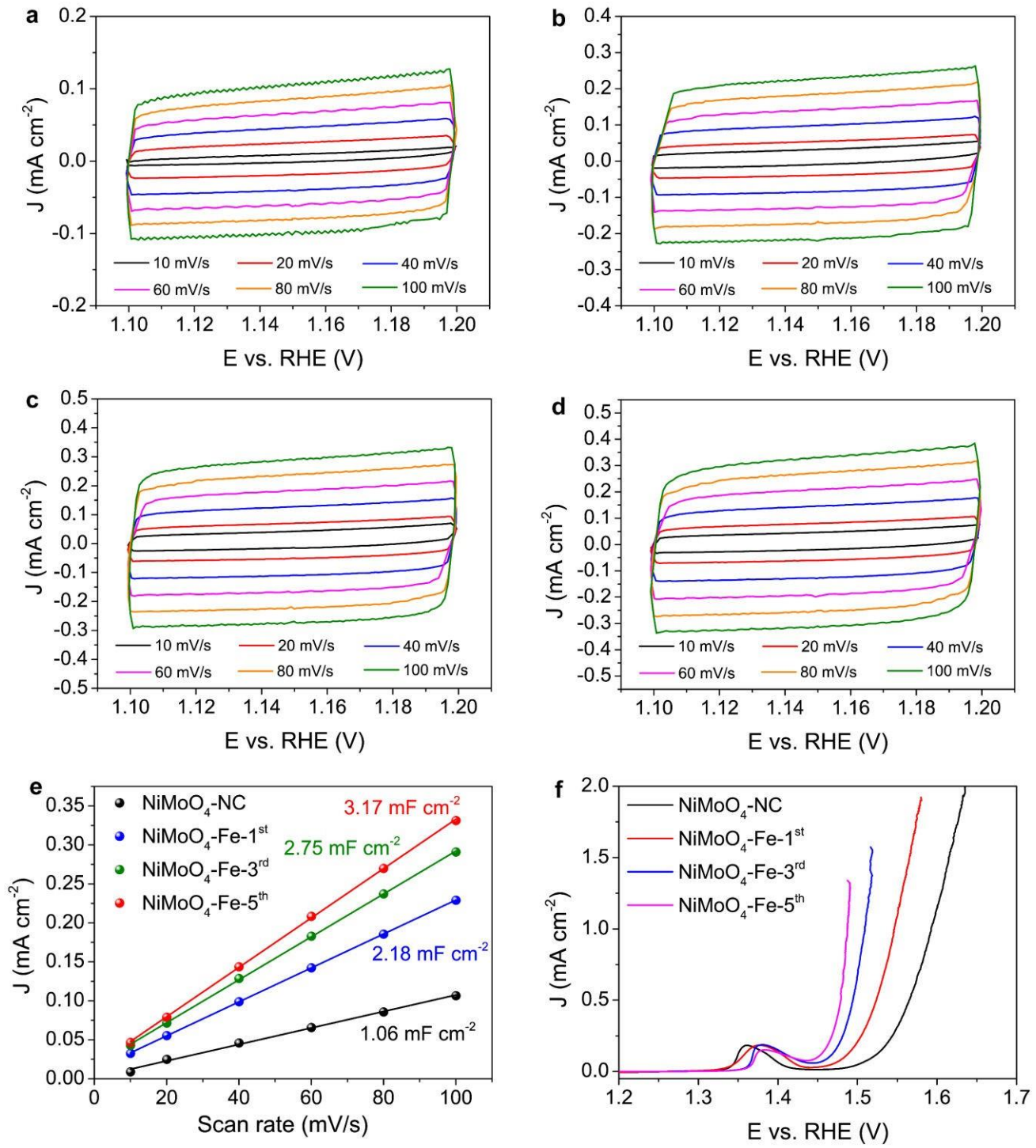

Figure S27. Cyclic voltammogram for **(a)** $NiMoO_4$-NC, **(b)** $NiMoO_4$-Fe-1st, **(c)** $NiMoO_4$-Fe-3rd and **(d)** $NiMoO_4$-Fe-5th. All voltammograms were collected in 1 M KOH. **(e)** Fitting results for the electrochemical double layer capacitance (C_{DL}) data and **(f)** normalized polarization curves for $NiMoO_4$-NC, $NiMoO_4$-Fe-1st, $NiMoO_4$-Fe-3rd and $NiMoO_4$-Fe-5th.

The electrochemical double-layer capacitance (Figure S27e) derived from cyclic voltammetry shows that multiple quenching increases the electrochemically active surface area (ECSA) due to the rough surface. By normalizing the polarization curves against the ECSA, $NiMoO_4$-Fe-5th possesses the best intrinsic OER activity (Figure S27f).

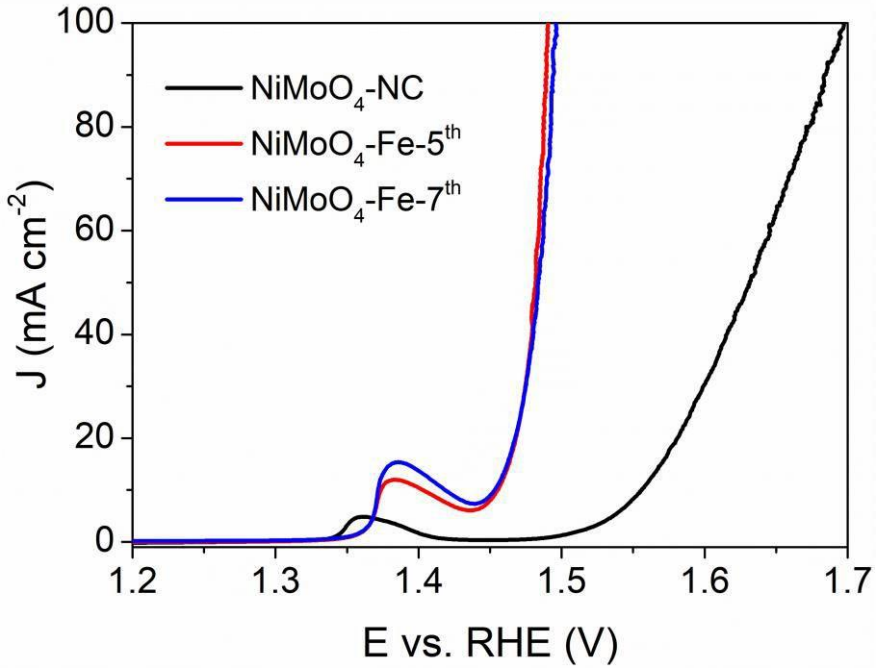

Figure S28. OER polarization curves in 1 M KOH solution for $NiMoO_4$ catalyst quenched in $Fe(NO_3)_3$ solution for seven times.

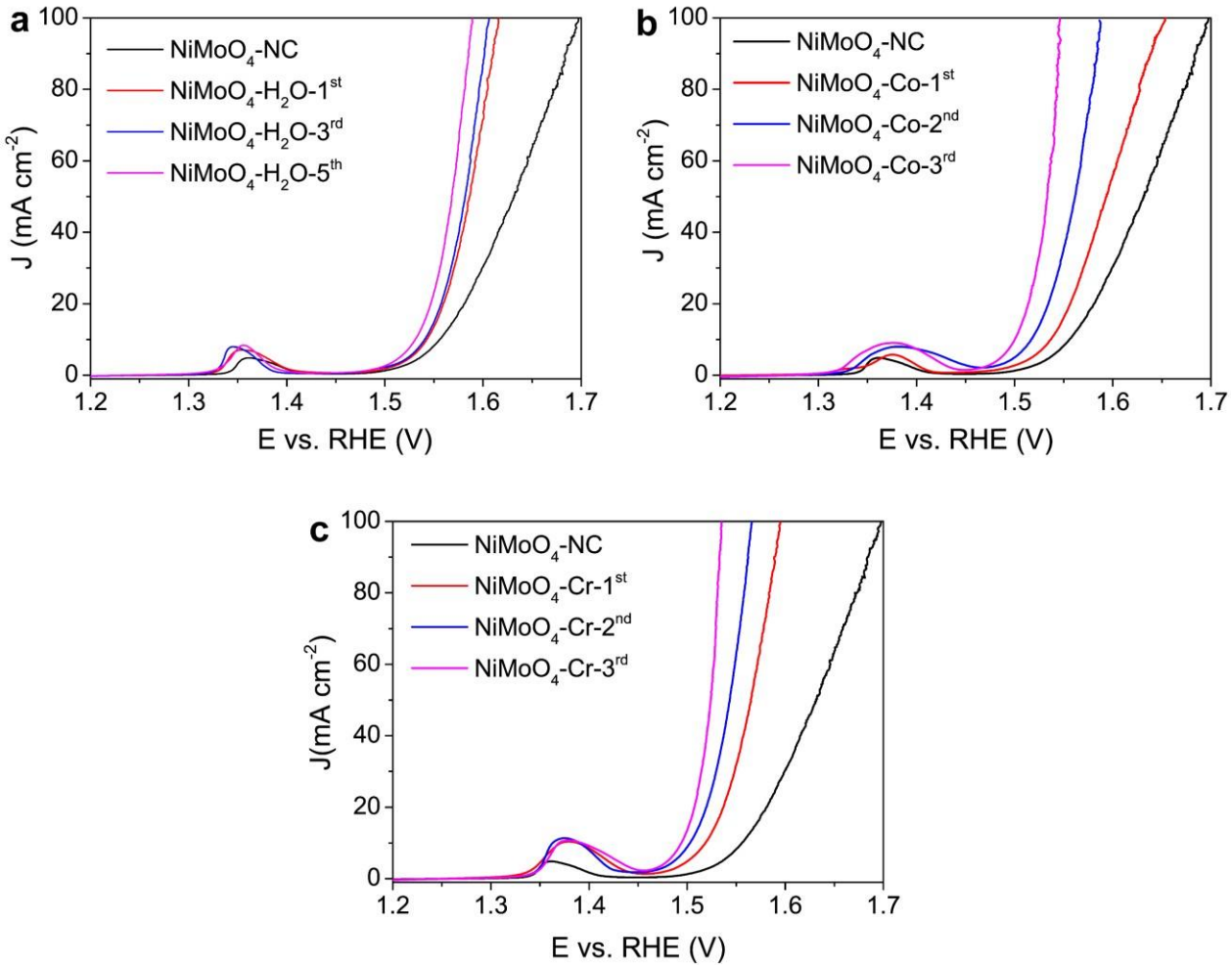

Figure S29. OER polarization curves in 1 M KOH solution for $NiMoO_4$ catalysts multiple quenched in **(a)** H_2O, **(b)** $Co(NO_3)_2$ and **(c)** $Cr(NO_3)_3$ solutions, respectively.

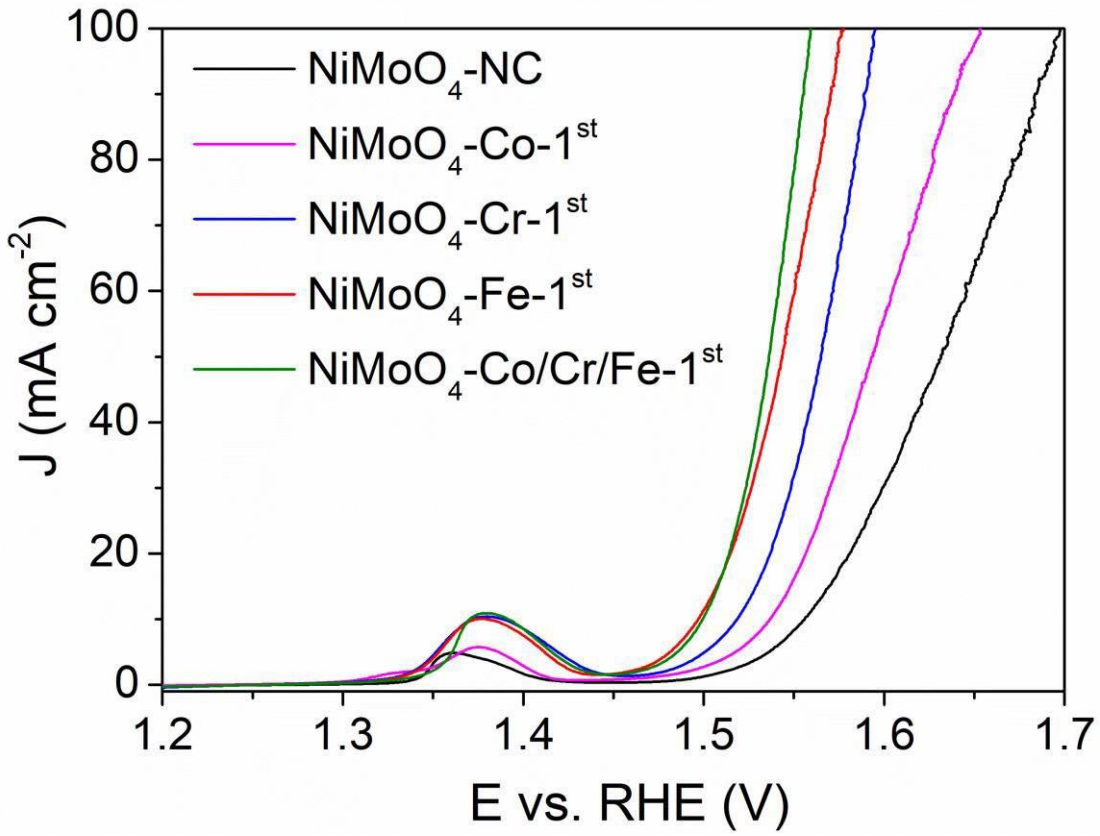

Figure S30. OER polarization curves in 1 M KOH solution for $NiMoO_4$ catalysts quenched once in a mixed solution containing $Co(NO_3)_2$, $Cr(NO_3)_3$ and $Fe(NO_3)_3$, compared with catalysts quenched in single salt solution and natural cooling.

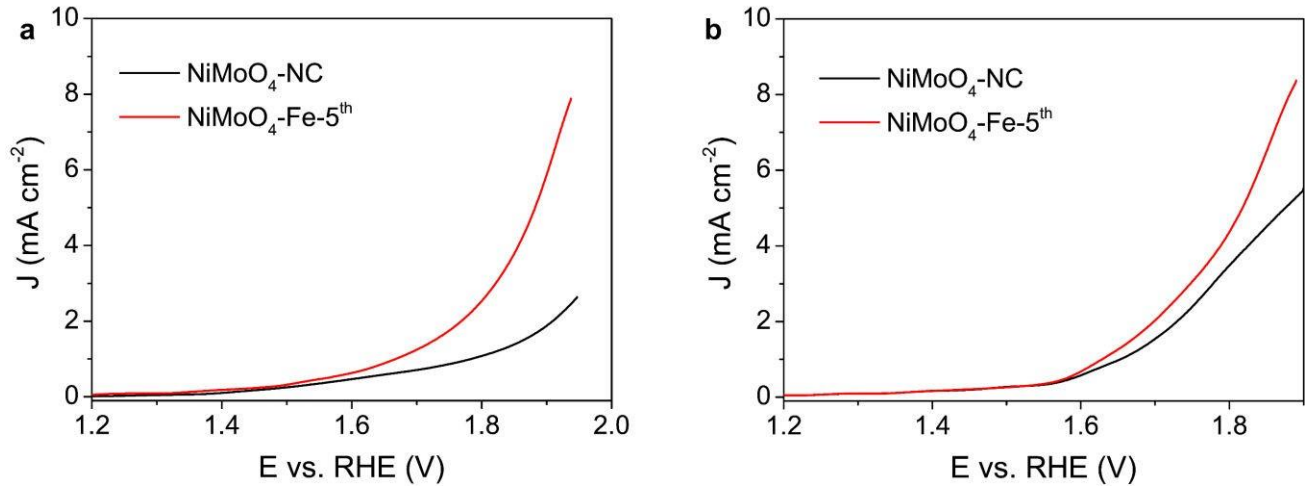

Figure S31. OER polarization curves for $NiMoO_4$-NC and $NiMoO_4$-Fe-5^{th} catalysts in **(a)** 0.5 M H_2SO_4 and **(b)** 0.1 M PBS (KH_2PO_4-K_2HPO_4 phosphate buffer solution) solution.

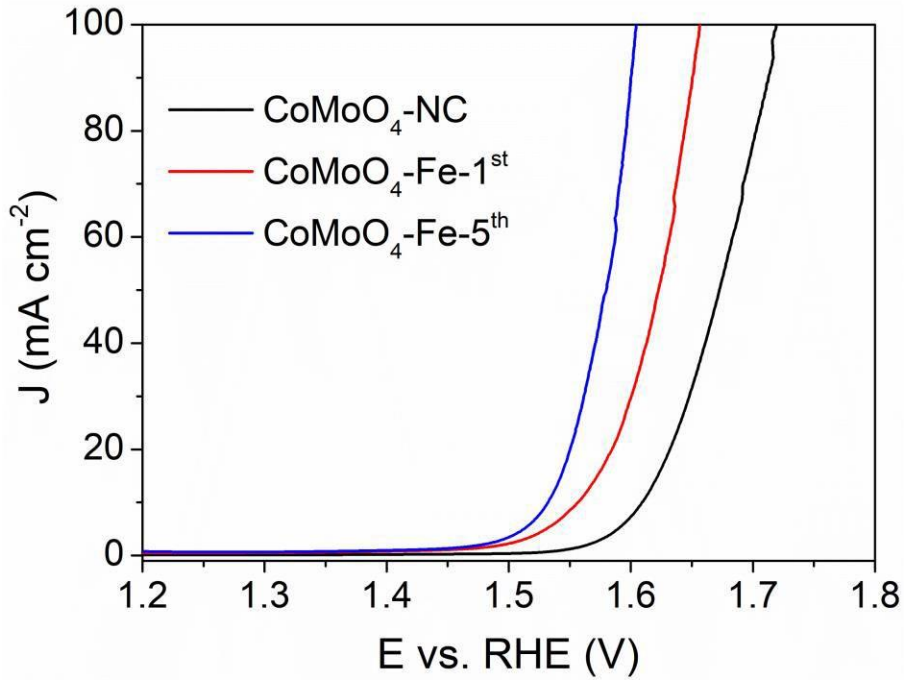

Figure S32. OER polarization curves in 1 M KOH solution for $CoMoO_4$-NC and $CoMoO_4$-Fe-5^{th} catalysts.

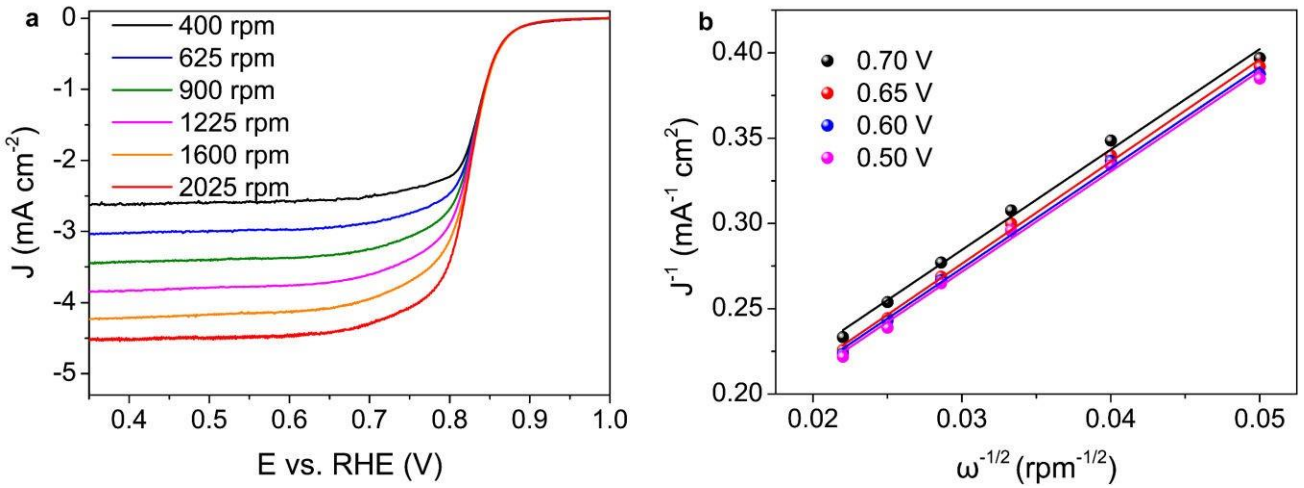

Figure S33. (a) ORR polarization curves in 1 M KOH solution recorded at different rotating speeds for $NiMoO_4$-Fe-5th, and **(b)** the corresponding Koutechky-Levich (K-L) plots.

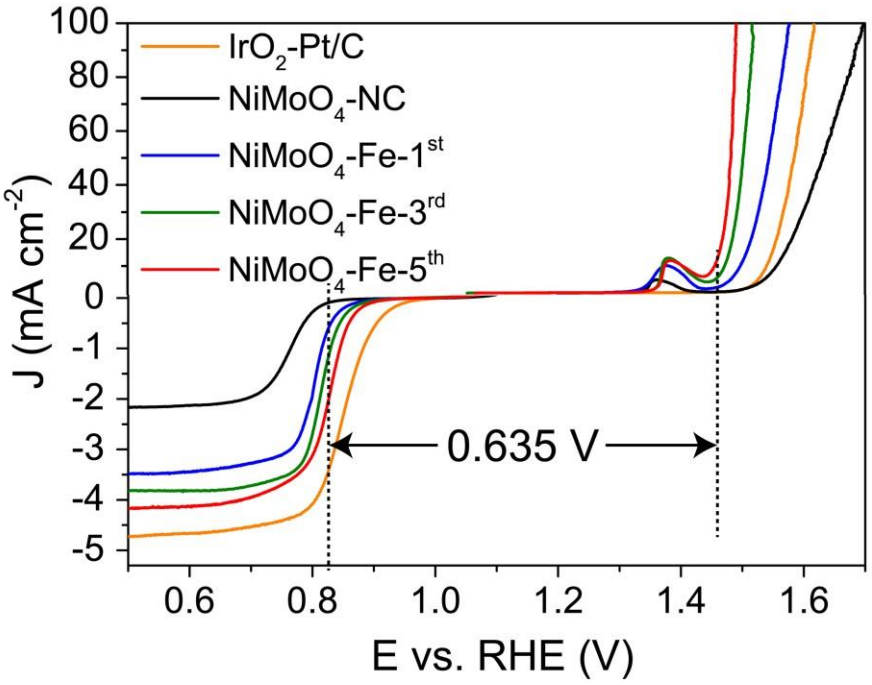

Figure S34. Bifunctional OER/ORR curves for the as-prepared catalysts in 1 M KOH solution.

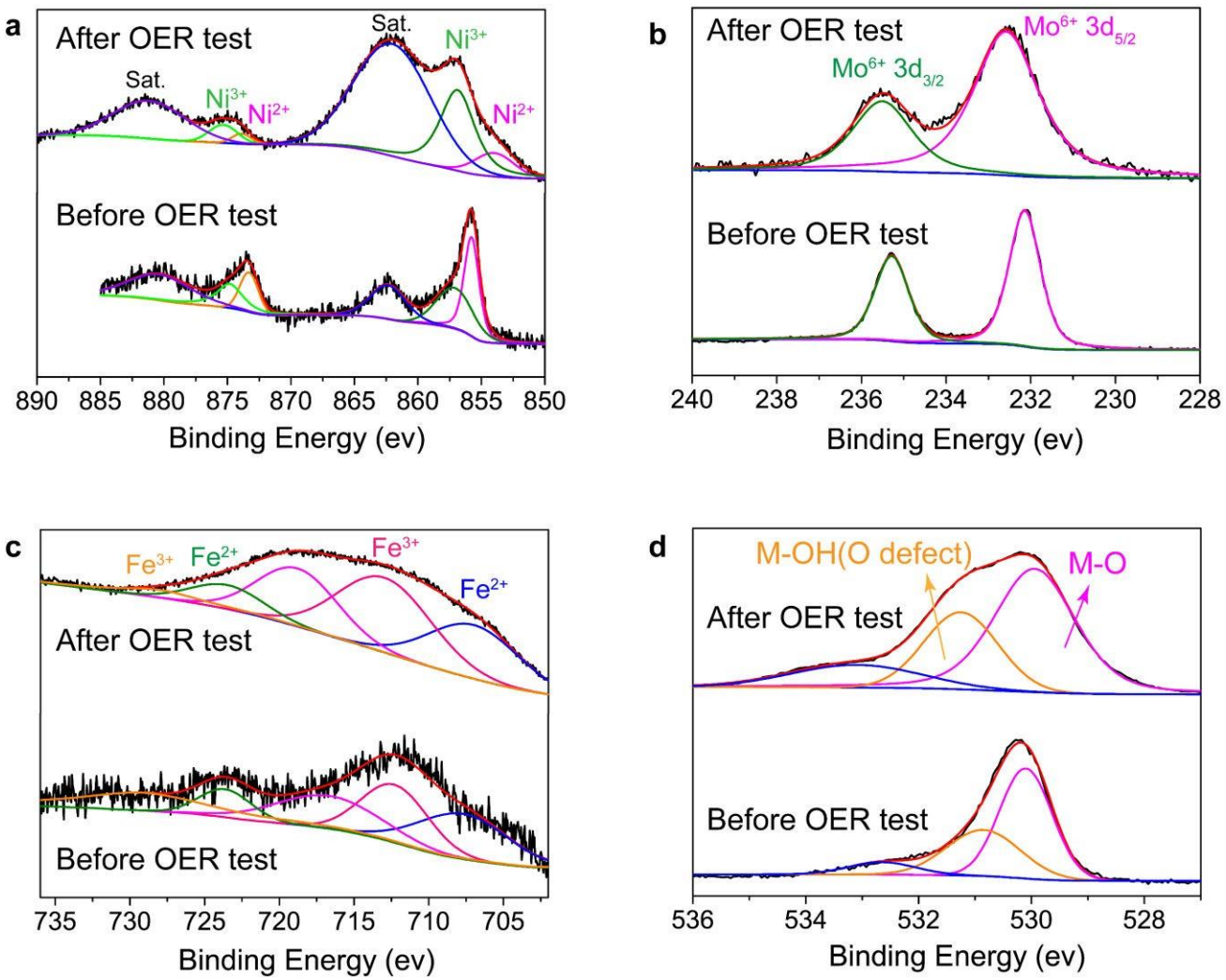

Figure S35. XPS spectra for $NiMoO_4$-Fe-5^{th} catalysts before and after CV test: **(a)** Ni 2p, **(b)** Mo 3d, **(c)** Fe 2p and **(d)** O 1s.

In order to analyze the surface composition of $NiMoO_4$-Fe-5^{th} catalyst after CV testing and identify the real active sites, we conducted ex-situ XPS and TEM characterizations. The XPS results show that the Ni 2p and Fe 2p characteristic peaks of $NiMoO_4$-Fe-5^{th} significantly change after OER testing, with more $Ni^{3+}$and Fe^{3+}, which may be attributed to the formation of NiOOH and FeOOH during the OER process. On the contrary, there is no significant change in the Mo 3d spectra. These changes indicate that both Ni and Fe may be the real active sites for OER. The O 1s spectra further demonstrate that oxyhydroxides are generated on the surface with more oxygen defects during OER.[8]

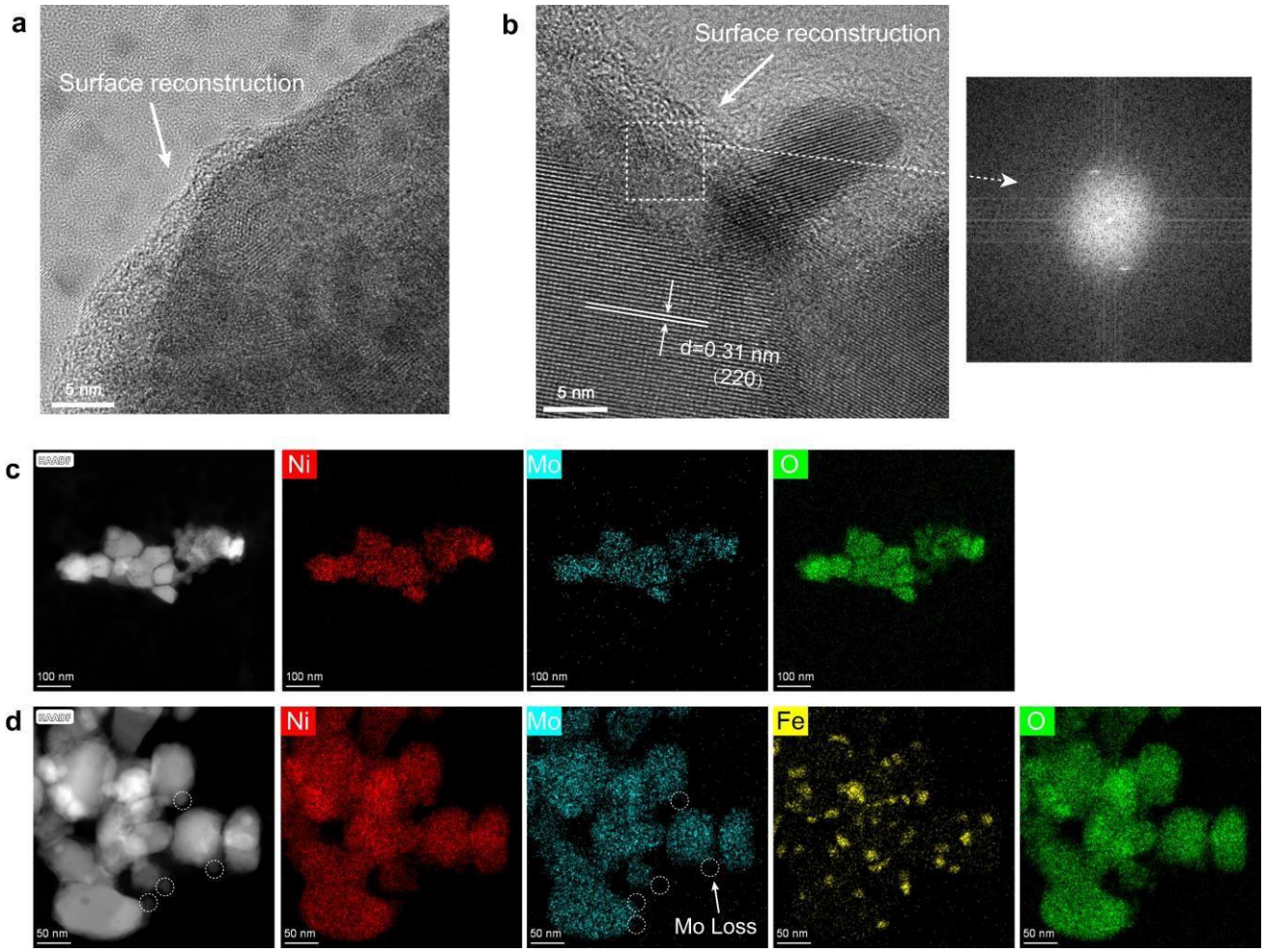

Figure S36. High-resolution TEM images and EDX elemental maps of **(a and c)** $NiMoO_4$-NC and **(b and d)** $NiMoO_4$-Fe-5th catalysts after CV test.

TEM images show that $NiMoO_4$-NC and $NiMoO_4$-Fe-5th catalysts undergo surface reconstruction during OER, forming highly active disordered species. Among them, $NiMoO_4$-Fe-5th has a thicker disordered layer, reaching about 10 nm. The EDX element maps show that catalysts still maintain the initial elemental distribution after OER testing, and Fe elements still aggregate in the small particles with significant Mo loss. Based on the above discussion, it is found that the quenching-induced surface interface structure can promote the surface reconstruction of $NiMoO_4$ and form more active sites. In addition, quenching-induced Fe doping further increases the active sites, which will be confirmed by the following theoretical calculations.

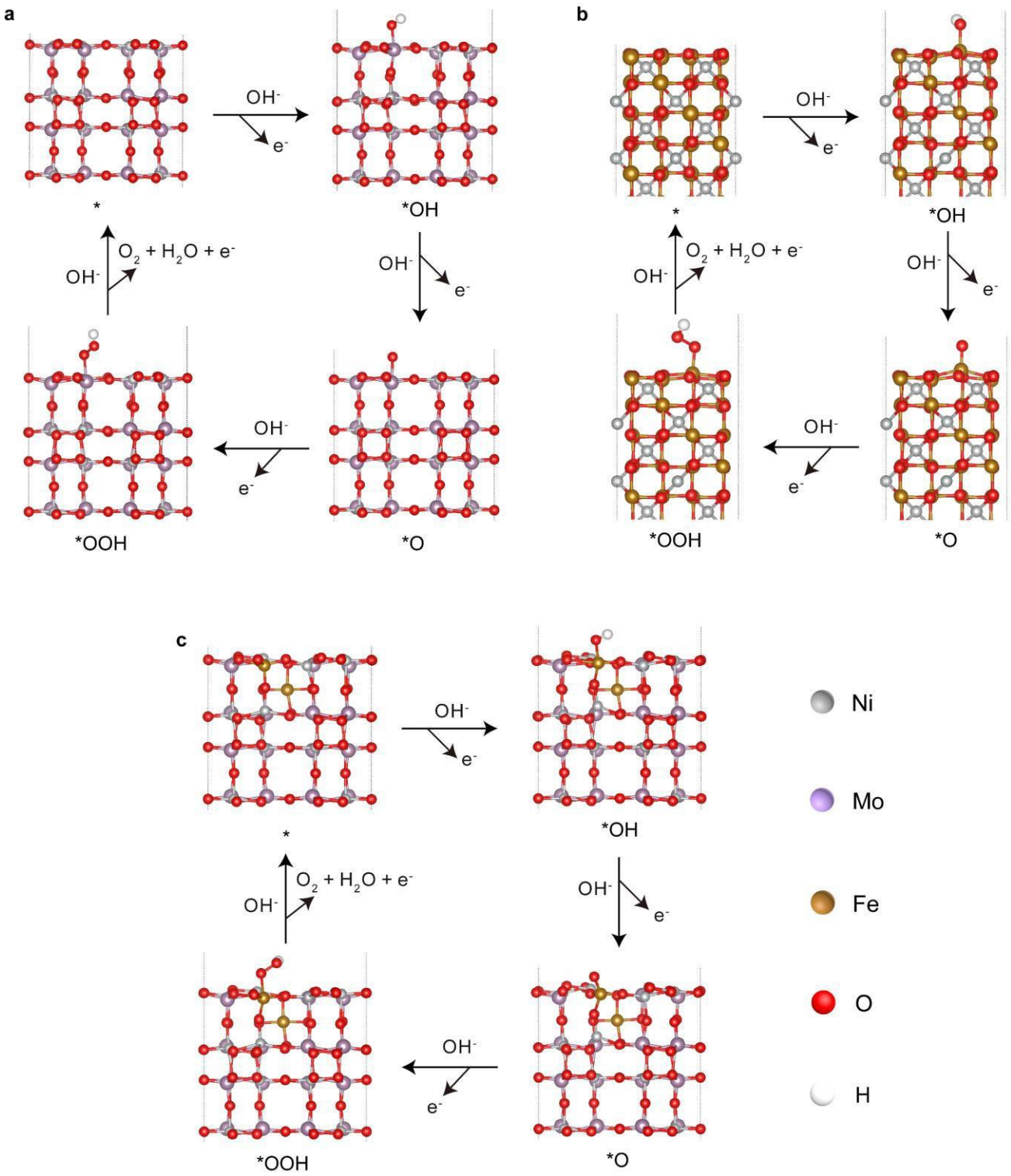

Figure S37. 4e-mechanism for the oxygen evolution reaction over **(a)** $NiMoO_4$-NC, **(b)** $NiFe_2O_4$ and **(c)** $NiMoO_4$-Fe-5th.

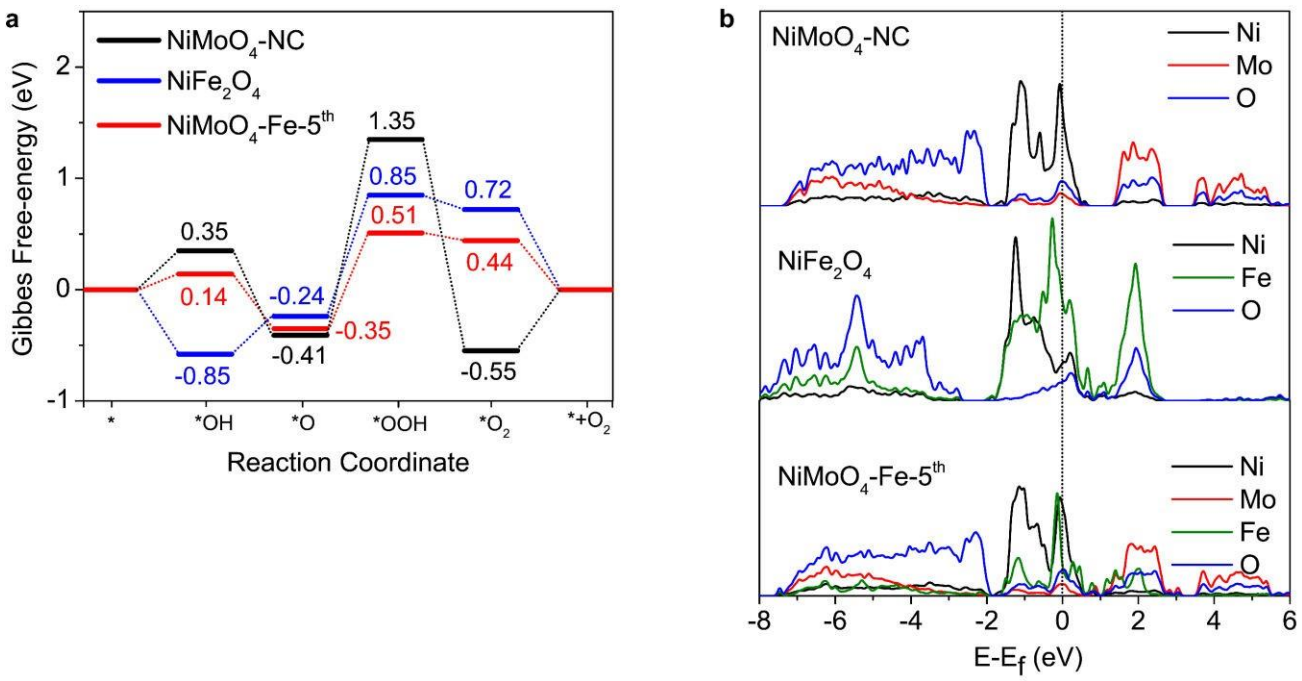

Figure S38. (a) Gibbs free energy diagram for the four electron OER transfer steps, and **(b)** density of states (DOS) of different catalysts.

To understand the effect of the quenching-induced heterostructure on catalytic activity, density functional theory (DFT) calculations were performed to understand the four-electron OER process. We simulated the $NiMoO_4/NiFe_2O_4$ heterointerface by inserting two Fe atoms on the surface of $NiMoO_4$ and calculated the conventional four-step OER mechanism (Figure S37), involving the stepwise oxidation of intermediates via *OH, *O, *OOH and O_2 (* is the active site). The free energy curves show that the potential determining step for all catalysts is the formation of *OOH (the third step) possessing the largest Gibbs free energy (Figure S38a). $NiMoO_4$-Fe-5^{th} has a lower value (0.51 eV) than $NiMoO_4$-NC (1.35 eV) and $NiFe_2O_4$ (0.85 eV). In other words, $NiMoO_4$-Fe-5^{th} needs a lower overpotential to drive water oxidation, suggesting that quenching-induced heterostructure enhances the intrinsic activity of the active site. To further understand the quenching-induced heterogeneous effect, the electronic structure of the catalysts was evaluated by DFT method. Compared with the large bandgap between the valence and conduction bands of $NiMoO_4$-NC, $NiMoO_4$-Fe-5^{th} has a narrower bandgap with a significant change in the conduction band structure (Figure S38b), explaining the improved the conductivity of the catalyst.

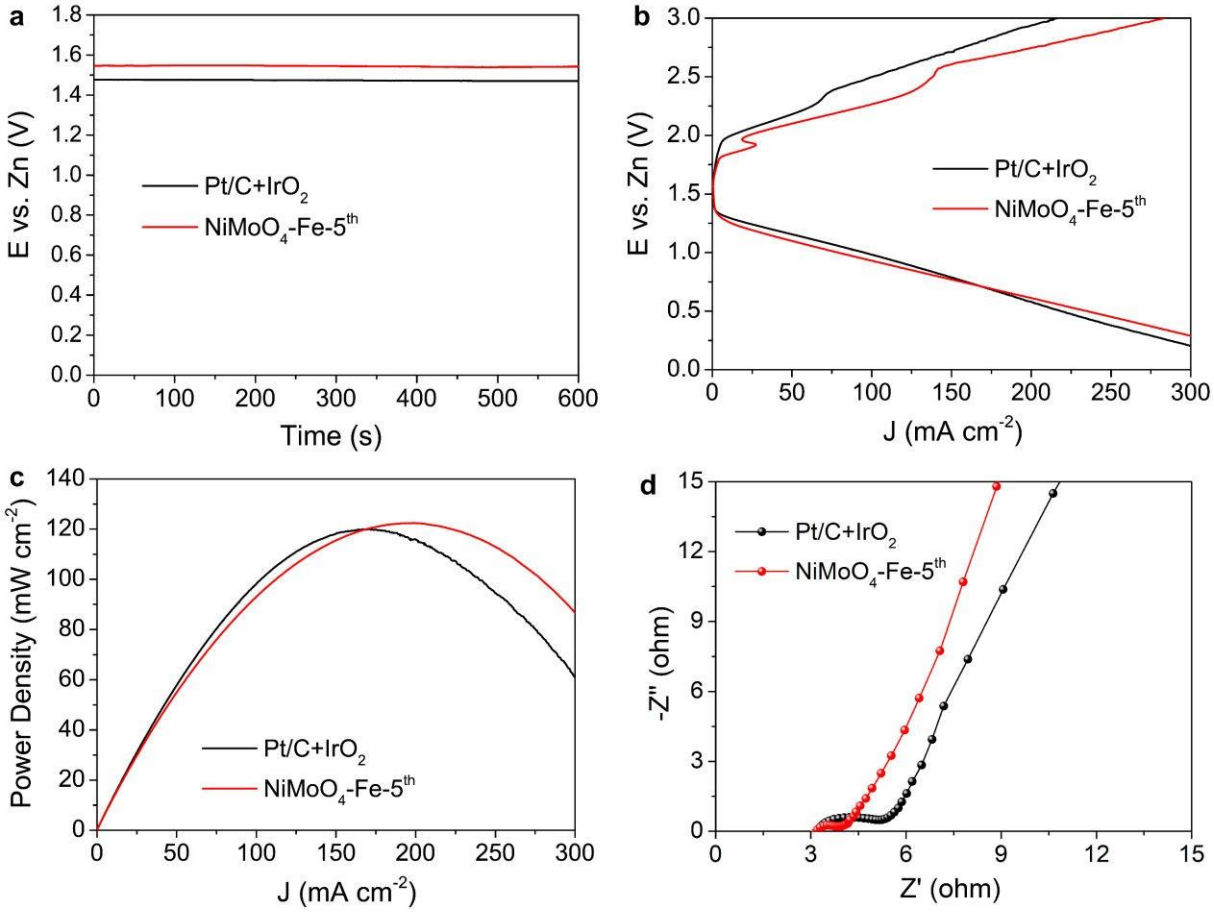

Figure S39. (a) Open-circuit voltage curves, **(b)** charge and discharge polarization curves, **(c)** power density plots and **(d)** electrochemical impedance spectroscopy for different aqueous zinc-air batteries using Pt/C+IrO_2 or $NiMoO_4$-Fe-5^{th} as the air-electrode catalysts.

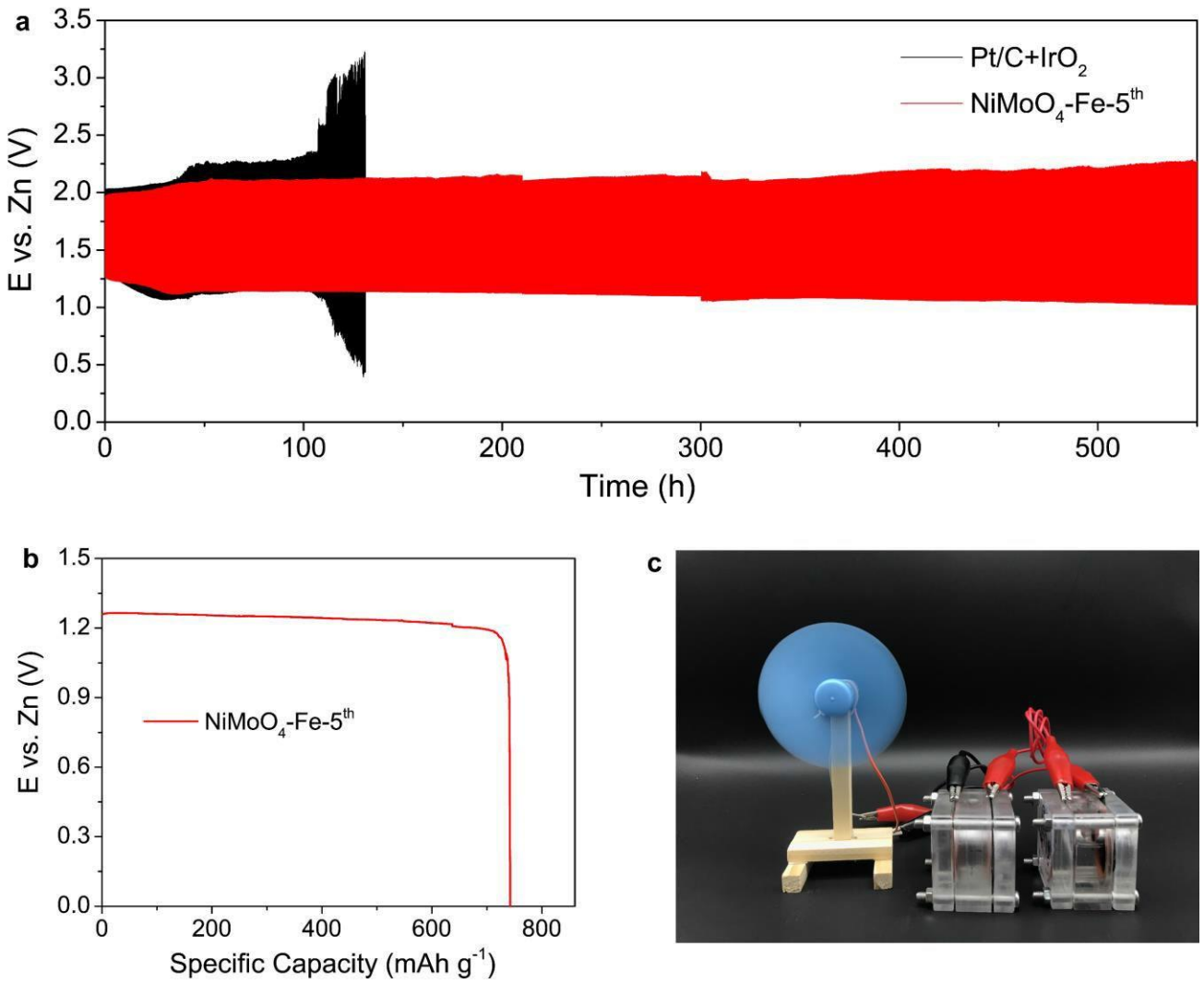

Figure S40. (a) Cyclic stability of different aqueous Zn-air battery at 5 mA cm^{-2}; **(b)** galvanostatic discharge curve of the aqueous ZAB battery based on $NiMoO_4$-Fe-5^{th} at 5 mA cm^{-2}, and the specific capacity is normalized by the mass of Zn consumed at the anode; **(c)** demonstration of two aqueous ZABs connected in series to power a fan.

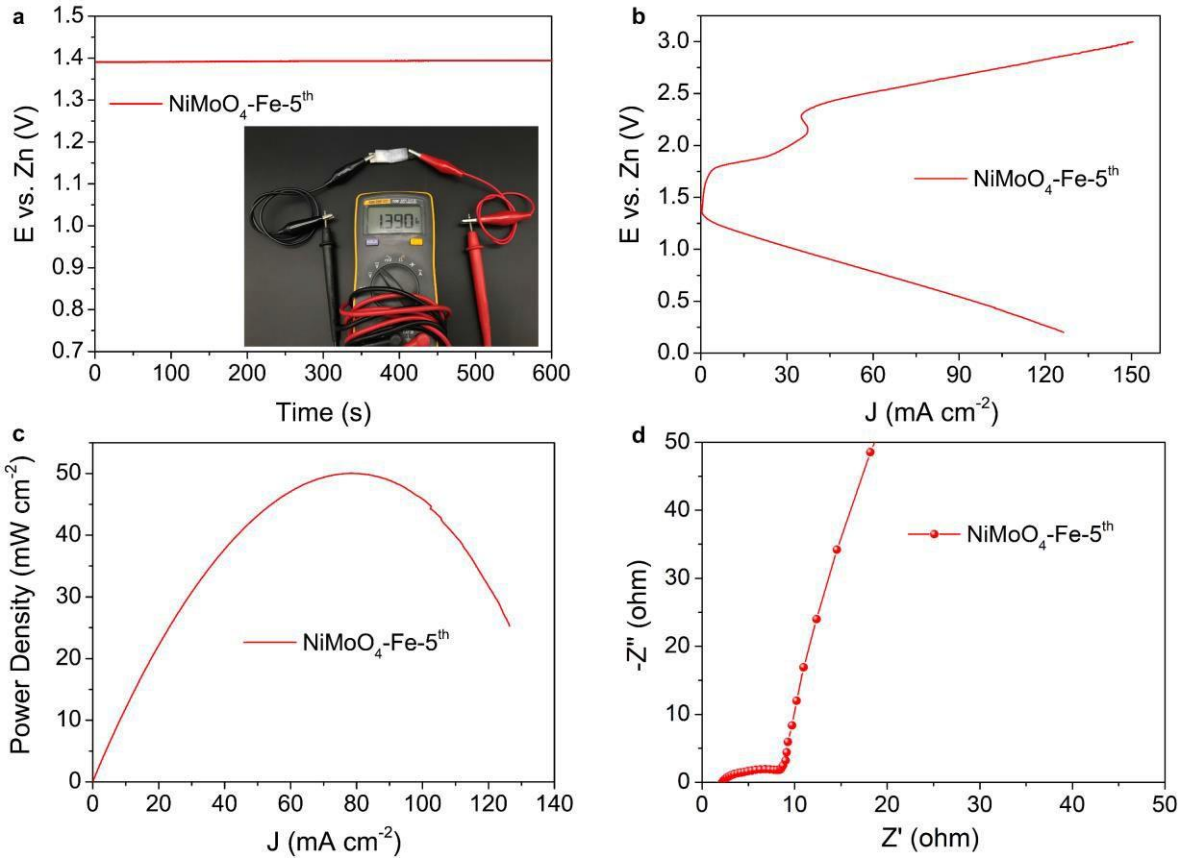

Figure S41. Performance of flexible solid-state zinc-air battery based on $NiMoO_4$-Fe-5^{th}: **(a)** open-circuit voltage curves, **(b)** charge and discharge polarization curves, **(c)** power density plots and **(d)** electrochemical impedance spectroscopy

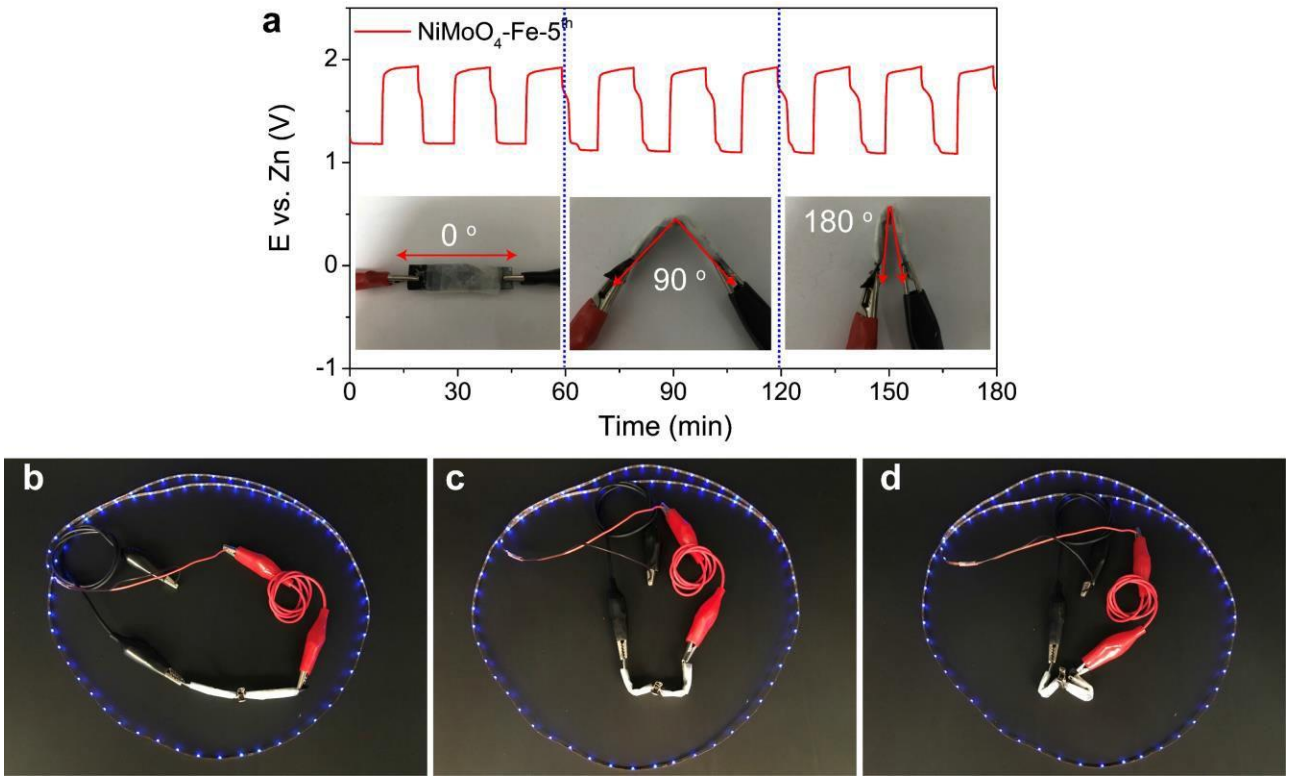

Figure S42. (a) Galvanostatic charge and discharge profiles for quasi-solid-state Zn-air battery containing $NiMoO_4$-Fe-5^{th} at 2 mA cm^{-2} and different bending angles; **(b)** Photograph of a flexible Zn-air battery powering LED lights.

Table S1: The metal contents in different catalysts determined by ICP-MS.

Samples	Content of Mo	Content of Ni	Content of Fe
$NiMoO_4$-NC	26.9%	24.9%	——
$NiMoO_4$-Fe-1st	25.0%	24.1%	0.6%
$NiMoO_4$-Fe-2nd	23.9%	24.9%	1.0%
$NiMoO_4$-Fe-3rd	22.7%	24.7%	1.2%
$NiMoO_4$-Fe-4th	22.6%	24.8%	1.5%
$NiMoO_4$-Fe-5th	22.1%	24.3%	1.7%

Table S2: Near surface region chemical composition of catalysts determined from XPS data.

Samples	O defect (O1s)	Ni^{3+}/Ni^{2+} (Ni 2p)	Fe^{3+}/Fe^{2+} (Fe 2p)
$NiMoO_4$-NC	12%	0.39	——
$NiMoO_4$-Fe-NC	19%	0.51	1.36
$NiMoO_4$-Fe-1st	22%	0.66	1.13
$NiMoO_4$-Fe-3rd	28%	0.79	1.02
$NiMoO_4$-Fe-5th	33%	0.86	0.95

Table S3. Comparison of the OER and ORR activities of the $NiMoO_4$-Fe-5th catalyst with other recently reported electrocatalysts in aqueous alkaline solution.

Catalysts	OER Overpotential (mV) at 10 mA/cm^2	ORR half-wave potential (V)	OER/ORR Overpotential gap (V)	Loading (mg cm^{-2})	Reference
$NiMoO_4$-Fe-5th	**227**	**0.822**	**0.635**	**0.255**	**This work**
CoO/hi-Mn_3O_4	378	0.800	0.808	0.250	Angew. Chem. Int. Ed. 2017, 56, 8539–8543
CoSA/NCs	303	0.870	0.663	0.210	Appl. Catal. B, 2022, 316, 121674.
NiFe/B, N-CNFs	290	0.840	0.680	0.240	Adv. Sci. 2022, 9, 2200753
MS-CoSA-N-C-800°C	310	0.860	0.680	0.255	ACS Nano 2022, 16, 8, 11944–11956
m-Fe/N-C@CNT	338	0.854	0.714	0.500	Appl. Catal. B, 2023, 327, 122443
PADN	290	0.76	0.76	0.106	Adv. Energy Mater. 2021, 11, 2102235
RRMM	260	0.830	0.66	0.416	Chem. Eng. J., 2023, 143760
V−Co_3O_4	351	0.821	0.760	0.250	ACS Catal. 2021, 11, 8097−8103
Co_2FeO_4/NCNTs	420	0.800	0.850	0.200	Angew. Chem. Int. Ed. 2019, 58, 1-7
MnO/Co/PGC	370	0.780	0.820	0.500	Adv. Mater. 2019, 31, 1902339
$Ni(S_{0.51}Se_{0.49})_2$@NC	320	0.830	0.720	0.260	Adv. Funct. Mater. 2022, 32, 2201944
Ni_{Oh}-Co_3O_4	380	0.840	0.77	0.354	ACS Energy Lett. 2023, 8, 1, 159–168
B-$CoSe_2$@CoNi LDH	250	0.810	0.670	——	Adv. Sci. 2022, 9, 2104522
$RuCoO_x$	275	0.855	0.650	0.400	Nano Lett. 2021, 21, 9633−9641

Table S4. Comparison of the Zn-air battery performance of the $NiMoO_4$-Fe-5th catalyst with other recently reported electrocatalysts.

Catalysts	Open circuit potential (V)	Power density (mW cm^{-2})	Specific capacity (mA h g_{Zn}^{-1})	Energy density (Wh kg_{Zn}^{-1})	Cycle (h), Current density, (mA cm^{-2})	References
$NiMoO_4$-Fe-5th	**1.56**	**123**	**745**	**916**	**442, 5**	**This work**
$Fe_{0.5}Co_{0.5}O_x$	1.44	86	709	806	120, 10	Adv. Mater. 2017, 29, 1701410
$CuCo_2O_4$/N-CNT	1.36	84	817	654	40, 20	Adv. Funct. Mater. 2017, 27, 1701833
CoZn-NC-700	1.42	152	578	694	64, 10	Adv. Funct. Mater. 2017, 27, 1700795
3DOM P-Co_3O_4–δ	1.45	70	761	890	250, 10	Energy Storage Mater. 41 (2021) 427–435
P–CoO@PWC-2	1.48	113	N.A.	N.A.	232, 10	Adv. Sci. 2021, 8, 2101314
ODAC-CoO-30	1.45	128	705	N.A.	150, 5	Adv. Funct. Mater. 2021, 31, 2101239
Gd_2O_3-Co/NG	N.A.	114.3	734.6	893	160, 10	Adv. Energy Mater. 2020, 10, 1903833
N-CoS_2 YSSs	1.41	81	744	922	165, 10	Adv. Sci. 2020, 7, 2001178
Ca-LaCoO3	1.44	106	793	793	220, 2	Energy Storage Mater. 42 (2021) 470–476
C-MOF-C2-900	1.46	105	741	N.A.	120, 2	30, 1705431
MCN	1.53	103	801	866	155, 2	Adv.Mater.2021, 33, 2007525
Co/N CCPC-3	1.48	87	707	N.A.	42 ,5	Nano Energy 2020, 79, 105487
$NiFe_2O_4$/$FeNi_2S_4$ HNSs	1.22	44.4	N.A.	N.A.	150, 0.5	J. Am. Chem. Soc. 2018, 140, 17624−17631
$NiFe_2O_4$/Ni_3S_4	1.28	129	437	N.A.	70, 10	Asian J. Chem., 2020, 15.21: 3568-3574
NiO/CoN PINWs	1.46	80	648	836	9, 50/1	ACS Nano 2017, 11, 2275−2283

References

1. G. Kresse and J. Hafner, *Phys. Rev. B*, 1994, **49**, 14251-14269.
2. G. Kresse and J. Hafner, *Phys. Rev. B*, 1993, **48**, 13115-13118.
3. J. P. Perdew, K. Burke and M. Ernzerhof, *Phys. Rev. Lett.*, 1996, **77**, 3865-3868.
4. G. Kresse and D. Joubert, *Phys. Rev. B*, 1999, **59**, 1758-1775.
5. A. O. Lyakhov, A. R. Oganov, H. T. Stokes and Q. Zhu, *Comput. Phys. Commun.*, 2013, **184**, 1172-1182.
6. C. W. Glass, A. R. Oganov and N. Hansen, *Comput. Phys. Commun.*, 2006, **175**, 713-720.
7. A. R. Oganov, A. O. Lyakhov and M. Valle, *Acc. Chem. Res.*, 2011, **44**, 227-237.
8. C. Liang, P. Zou, A. Nairan, Y. Zhang, J. Liu, K. Liu, S. Hu, F. Kang, H. J. Fan and C. Yang, *Energy Environ. Sci.*, 2020, **13**, 86-95.